Adrenomedullin-RAMP2 and -RAMP3 systems regulate cardiac homeostasis during cardiovascular stress

Nanqi Cui[1], Takayuki Sakurai[1, 2], Akiko Kamiyoshi[1, 2], Yuka Ichikawa-Shindo[1], Hisaka Kawate[1], Megumu Tanaka[1], Masaaki Tanaka[1], Yangxuan Wei[1], Shinji Kakihara[1], Yunlu Zhao[1], Kohsuke Aruga[1], Hiroyuki Kawagishi[3, 4], Tsutomu Nakada[5], Mitsuhiko Yamada[3], Takayuki Shindo[1, 2]

[1]Department of Cardiovascular Research, Shinshu University School of Medicine, Japan
[2]Department of Life Innovation, Institute for Biomedical Sciences, Interdisciplinary Cluster for Cutting Edge Research, Shinshu University, Japan
[3]Department of Molecular Pharmacology, Shinshu University School of Medicine, Japan
[4]Department of Biotechnology, Institute for Biomedical Sciences, Interdisciplinary Cluster for Cutting Edge Research, Shinshu University, Japan
[5]Department of Instrumental Analysis, Research Center for Supports to Advanced Science, Shinshu University, Japan

Short running head: Regulation of cardiac homeostasis by RAMP2 and 3

Number of text pages 40
Number of tables 1
Number of figures 14
Number of supplementary figures 9

Address for correspondence
Takayuki Shindo, MD, PhD
Department of Cardiovascular Research,
Shinshu University School of Medicine
Asahi 3-1-1, Matsumoto, Nagano, 390-8621, Japan
Tel: +81-263-37-2578
Fax: +81-263-37-3437
Email: tshindo@shinshu-u.ac.jp

Disclosures:

Sources of funding

This work was supported by JSPS KAKENHI Grant Number 18KT0005.

Authors' contributions

NC carried out the experiments and wrote the manuscript. TS and AK generated genetically engineered mice. YI, HK and MT helped histological analysis. MT helped gene expression analysis. YW and SK helped Western blot analysis. YZ and KA helped TAC operation. HK, TN and MY lectured Ca2+ imaging analysis. TS planed the experiments and supervised the manuscript.

Conflicts of interest

The authors declare no conflicts of interest associated with this manuscript.

Abstract

Adrenomedullin (AM) is a peptide hormone with multiple physiological functions, which are regulated by its receptor activity-modifying proteins, RAMP2 and RAMP3. We previously reported that AM or RAMP2 knockout (AM-/-, RAMP2-/-) is embryonically lethal in mice, whereas RAMP3-/- mice are apparently normal. AM, RAMP2 and RAMP3 are all highly expressed in the heart; however, their functions there are not fully understood. Here, we analyzed the pathophysiological functions of the AM-RAMP2 and AM-RAMP3 systems in hearts subjected to cardiovascular stress.

Cardiomyocyte-specific RAMP2-/- (C-RAMP2-/-) and RAMP3-/- showed no apparent heart failure at base line. After one week of transverse aortic constriction (TAC), however, C-RAMP2-/- exhibited significant cardiac hypertrophy, decreased ejection fraction and increased fibrosis as compared to wild-type mice. Both dP/dtmax and dP/dtmin were significantly reduced in C-RAMP2-/-, indicating reduced ventricular contractility and relaxation. Exposing C-RAMP2-/- cardiomyocytes to isoproterenol enhanced their hypertrophy and oxidative stress as compared to wild-type cells. C-RAMP2-/- cardiomyocytes also contained fewer viable mitochondria and showed reduced mitochondrial membrane potential and respiratory capacity. RAMP3-/- also showed reduced systolic function and enhanced fibrosis after TAC, but those only became apparent after 4 weeks. A reduction in cardiac lymphatic vessels was the characteristic feature in RAMP3-/-.

These observations indicate the AM-RAMP2 system is necessary for early adaptation to cardiovascular stress through regulation of cardiac mitochondria. AM-RAMP3 is necessary for later adaptation through regulation of lymphatic vessels. The AM-RAMP2 and AM-RAMP3 systems thus play separate critical roles in the maintenance of cardiovascular homeostasis against cardiovascular stress.

Non-standard Abbreviations

AM: Adrenomedullin

RAMP: Receptor activity-modifying protein

CLR: Calcitonin receptor-like receptor

KO: Knockout

DI-C-RAMP2-/-: Inducible cardiac myocyte-specific RAMP2-/-

C-RAMP2-/-: Congenital cardiac myocyte-specific RAMP2-/-

TAC: Transverse aortic constriction

ISO: Isoproterenol

BNP: Natriuretic peptide type B

PGC-1α: peroxisome proliferator-activated receptor γ coactivator-1α

PGC-1β: peroxisome proliferator-activated receptor γ coactivator-1β

BAX: Bcl2-associated X protein

BCL-2: Bcl2, apoptosis regulator

CREB: cAMP response element binding protein

Cx43: Connexin 43

Key Words:

Adrenomedullin ■ Heart failure ■ Cardiac hypertrophy ■ Cardiac fibrosis ■ Mitochondria ■ Lymphatic vessel

Introduction

Cardiovascular diseases are responsible for more than 30% of all deaths worldwide (1). Despite considerable progress in the treatment of cardiovascular diseases, there is a growing need for more efficient therapies that, for example, increase the long-term beneficial effects of chronic pharmacological therapy while eliminating toxicity (2). Endogenous bioactive peptides and their receptors within the cardiovascular system play pivotal roles in maintaining circulatory homeostasis, and they are now recognized to be important drug targets for the treatment of various diseases (3). Adrenomedullin (AM) is a 52-amino acid vasodilating peptide hormone first identified from human pheochromocytoma (4). AM is mainly secreted in cardiovascular system; however, it is now known to be widely distributed in numerous tissues and organs (5). Moreover, subsequent studies revealed that in addition to its vasodilating effect, AM functions as both a local autocrine/paracrine mediator (6) and a circulating hormone (7), and exerts cardiotonic (8), natriuretic (9) and antioxidative (10,11) effects, among others. AM levels in the blood are increased in hypertension (7), heart failure (12,13) and myocardial infarction (14), and the magnitude of the elevation is proportional to the severity of the disease, which suggests its central involvement in these cardiovascular diseases.

We previously observed in mice that homozygous knockout (KO) of AM (AM-/-) is embryonically lethal at midgestation with systemic edema and bleeding that are mainly caused by abnormal vascular development (15,16). These observations made it clear that AM is essential for proper development of the vascular system. Conversely, transgenic mice overexpressing AM exhibit resistance to various forms of organ damage (16,17), suggesting AM exerts organ protective effects.

We have been focusing on AM's receptor system. AM is a member of the calcitonin superfamily and acts via a G protein-coupled 7-transmembrane domain receptor, calcitonin receptor-like receptor (CLR) (18). The specificity of CLR for its ligands is regulated by a group of three receptor activity-modifying proteins, RAMP1,

-2 and -3, and the combination of CLR with RAMP2 or RAMP3 is known to have high affinity for AM (19). Interestingly, among RAMP KO mice, only RAMP2 homozygotic KO mice (RAMP2-/-) die midgestation and reproduce the phenotypes observed in AM-/- mice (20). RAMP2 thus appears to be the key determinant of AM's function during vascular development. We therefore generated vascular endothelial cell-specific RAMP2 KO mice (E-RAMP2-/-) and found that most E-RAMP2-/- died perinatally (21). In the surviving adult E-RAMP2-/- mice, vasculitis and organ fibrosis occurred spontaneously, clearly indicating endogenous RAMP2 is essential for vascular integrity.

Although CLR with RAMP3 also has high affinity of AM, in contrast to RAMP2-/- KO, homozygotic RAMP3 KO (RAMP3-/-) mice, are born with no major vascular abnormalities (22). On the other hand, we found that drainage of subcutaneous lymphatic vessels was delayed in adult RAMP3-/- mice, which also showed more severe interstitial edema than wild-type mice in a postoperative lymphedema model. These results suggest that whereas the AM-RAMP2 system mainly regulates homeostasis of blood vessels, the AM-RAMP3 system mainly regulates homeostasis of lymphatic vessels.

AM, RAMP2 and RAMP3 are also highly expressed in the heart from embryo to adulthood, but their functions there are still not fully understood. Our aim in the present study was to clarify the pathophysiological actions of the AM-RAMP2 and AM-RAMP3 systems in the adult heart. As RAMP2-/- KO are embryonic lethal, we generated KO line in which RAMP2 gene was congenitally deleted in a cardiomyocyte-specific manner (C-RAMP2-/-). In the present study, we induced cardiovascular stress using transverse aortic constriction (TAC) in C-RAMP2-/- and RAMP3-/- mice and analyzed the roles of the endogenous AM-RAMP2 and AM-RAMP3 systems in the adaptive compensatory responses to cardiovascular stress.

Methods and materials

Animals

RAMP3 KO mice (RAMP3-/-) were previously generated in our group (22). Congenital cardiomyocyte-specific RAMP2 KO (C-RAMP2-/-) mice were generated by cross breeding RAMP2 flox mice (20) with cardiac-specific αMHC-Cre transgenic mice (23). Eight-week-old male KO mice and their wild-type littermates (αMHC-Cre (-) / RAMP2 flox/flox mice) were used in this study. Before the study, we confirmed that morphology and function of the heart before and after transverse aortic constriction (TAC) was not different between αMHC-Cre (+) / RAMP2 flox (-) mice and αMHC-Cre (-) / RAMP2 flox/flox mice (Supplementary Figure 1) (24).

The background of mice used in this study was C57BL/6J. All mice were maintained according to a strict procedure under specific pathogen-free conditions in an environmentally controlled (12 h light/dark cycle; room temperature, 22 ± 2 °C) breeding room at the Division of Laboratory Animal Research, Department of Life Science, Research Center for Human and Environmental Sciences, Shinshu University. All animal experiments were conducted in accordance with the ethical guidelines of Shinshu University, Declaration of Helsinki and NIH Guide for the Care and Use of Laboratory Animals. All of the experiments were approved by the Shinshu University Ethics Committee for Animal Experiments. Before all invasive procedures, mice were anesthetized through inhalation of 1.4% isoflurane (Sumitomo Dainippon Pharma, Tokyo, Japan). Mice were euthanized by isoflurane overdose.

TAC model

TAC was performed according as previously described (25,26). Eight-week-old mice were anesthetized through inhalation of 1.4% isoflurane (Sumitomo Dainippon Pharma, Tokyo, Japan), intubated, and then ventilated with a rodent ventilator (Shinanoseisakusho, Tokyo, Japan) connected to an inhalation anesthesia apparatus

(Bio Research Center, Nagoya, Japan and Nitto Kohki, Tokyo, Japan). The chest was opened, and following blunt dissection through the intercostals muscles, the thoracic aorta was identified. An 8-0 nylon suture was placed around the transverse aorta and tied with blunt needle (27G), which was subsequently removed. After closing the chest and confirming that the mouse was awake, follow-up observations were made after 1 week and 4 weeks.

Echocardiography

Mice were set in a supine position, and echocardiography was performed using a Vevo 2100 imaging system (VisualSonics, Toronto, Canada). Standard imaging planes, M-mode, Doppler, and functional calculations were according to American Society of Echocardiography guidelines. Heart rates during echocardiographic studies were maintained in the range of 450 to 500 bpm.

Hemodynamic measurement

Under anesthesia, mice were set in a supine position, intratracheally intubated and connected to a rodent ventilator. After the chest was opened, the apical portion of left ventricle was punctured with a 27-gauge needle (a cautery was used to minimize bleeding), and a 1.4-Fr high-fidelity pressure transducer (model SPR-671, Millar Instruments, Houston, TX) connected to a pressure control unit (model TCB-500, Millar Instruments) was inserted into the left ventricle. Left ventricular (LV) pressure and aortic pressure were recorded using a data acquisition system (PowerLab 4/20 with BioAmp ML-132, ADInstruments, Sydney, Australia) and data analysis software (LabChart Ver 8 with Blood pressure module Ver 1.4, ADInstruments).

Histological examination

Heart sections were fixed in 4% formalin neutral buffer, embedded in paraffin, and cut into 5-μm-thick sections. Some sections were used for hematoxylin/eosin and

Masson trichrome staining. Immunohistochemical staining was performed using anti-LYVE-1 (Cat# 103-PA5, Relia Tech GmbH, Wolfenbüttel Germany, RRID:AB_2783787) (27), anti-CD31 (Cat# 557355, BD Biosciences, San Jose, CA, RRID:AB_396660) (28) and ant-Cx43 (Cat# C6219, Sigma, Saint Louis, MO, RRID:AB_476857) (29) antibodies. Cell borders were detected using rhodamine wheat germ agglutinin (WGA) (Vector Laboratories, Burlingame, CA). Capillary vessels were detected using Alexa Fluor 568-conjugated Griffonia bandeiraea simplicifolia isolectin B4 (Thermo Fisher Scientific, Waltham, MA). Apoptosis was detected using the terminal deoxynucleotidyl transferase (TdT)-mediated deoxyuridine triphosphate (dUTP)-digoxigenin nick end labelling (TUNEL) method with an Apoptosis In Situ Detection Kit (Chemicon, Temecula, CA, USA). Mitochondrial enzymatic activity was evaluated by succinate dehydrogenase (SDH) staining. Ten-μm-thick cryosections were incubated with a mixture of nitroblue tetrazolium (NBT), sodium succinate and phosphate buffered saline (PBS). The inspections were performed using a microscope (BZ-9000; Keyence, Osaka, Japan). Quantification was performed using a BZ analyzer (Keyence).

Transmission electron microscopy

Specimens were fixed in 2% glutaraldehyde (pH 7.2) and 4% osmium tetroxide, embedded in epoxy resin (Epok) 812 (Oken Shoji, Tokyo, Japan), cut into ultrathin sections, double-stained with uranyl acetate and lead citrate, and examined in an electron microscope (JEM-1010; JEOL, Tokyo, Japan).

Real-time qPCR analysis

Total RNA was prepared using TRI REAGEN (Molecular Research Center, Cincinnati, OH) and a DNA-free DNA Removal kit (Ambion, Naugatuck, CT) according to the manufacturer's instructions. For cDNA synthesis, RNA was reverse-transcribed using a High Capacity cDNA Reverse Transcription Kit (Applied

Biosystems, Foster City, CA). PCR primers and probes were designed using NCBI Primer-BLAST (https://www.ncbi.nlm.nih.gov/tools/primer-blast/) and synthesized by Integrated DNA Technologies (Coralville, IA). The primers and probes used are listed in Table 1. qRT-PCR was performed using SYBR Green (Toyobo, Osaka, Japan) or Realtime PCR Master Mix (Toyobo) and TaqMan probes (MBL, Aichi, Japan) on an ABI Prism 7300 Sequence Detection System (Applied Biosystems). The cycling conditions were 50°C for 2 min and 95°C for 2 min, followed by 40 cycles of 95°C for 15 s and 60°C for 1 min. Relative mRNA levels were normalized to mouse glyceraldehyde-3-phosphate dehydrogenase mRNA (Pre-Developed TaqMan assay reagents; Applied Biosystems) and calculated using the comparative cycle threshold method (ΔΔCt).

Ca^{2+} imaging

Isolation of adult cardiomyocytes from SHAM or TAC-treated mice and Ca^{2+} imaging were performed as previously described (30,31). Briefly, cardiomyocytes plated on laminin-coated glass bottom dishes were incubated with 5 μM Fluo-4-AM (Dojindo, Kumamoto, Japan) plus 0.01% CremophorEL (Sigma-Aldrich, St. Louis, MO) and 0.02% bovine serum albumin (Sigma) in serum-free DMEM for 45 min at 37ºC, which was sufficient for de-esterification. The Fluo-4-loaded cardiomyocytes were superfused with modified Tyrode solution (136.5 mM NaCl, 5.4 mM KCl, 1.8 mM $CaCl_2$, 0.53 mM $MgCl_2$, 5.5 mM HEPES, and 5.5 mM glucose, pH 7.4) at room temperature and paced with 1 ms pulses of 50 V at 0.5 Hz. Fluorescence images were acquired using a LSM 7 LIVE laser scanning microscope (Carl Zeiss, Oberkochen, Germany). Ca^{2+} transients were evaluated based on the changes in Fluo-4 fluorescence within individual cardiomyocytes. An increment in fluorescence intensity from a baseline (ΔF) was normalized to the baseline intensity (F_0) ($\Delta F/F_0$).

Isolation of neonatal cardiomyocytes

Primary cardiomyocytes were cultured from P0 neonatal mice. Collected hearts were washed in PBS, minced, and incubated with 0.25% trypsin-EDTA (Thermo Fisher Scientific, Waltham, MA) for 15 min at 37°C with agitation. During this period, the digestion buffer was replaced 3 times. Culture dishes were incubated for 60 min to remove non-myocytes. Unattached viable cells were collected and cultured on gelatin-coated dishes at 37°C in Minimum Essential Medium supplemented with 10% FBS and penicillin/streptomycin. Using this protocol, we consistently obtained cell populations containing at least 80% cardiomyocytes. Before the following experiments, we refreshed the culture medium of the cardiomyocytes, which were attached to the gelatin-coated dishes. Neonatal cardiomyocytes were treated for 24 h with 10 μM isoproterenol (ISO) or control medium (CONT). "N" in the cellular study represents the number of repeated experiments.

Detection of oxidative stress in cardiomyocytes

Neonatal cardiomyocytes were seeded onto collagen (Cellmatrix Type I -C, Wako, Osaka, Japan)-coated glass dishes (Iwaki, Tokyo, Japan). After 72 h, the cells were stained with dihydroethidium (DHE) (Sigma-Aldrich) and Hoechst 33342 (Thermo Fisher Scientific) for 30 min at 37°C in the dark to visualize cytosolic superoxide. Other cells were stained with MitoSOX Red (Thermo Fisher Scientific) and Hoechst 3334 for 10 minutes at 37˚C in the dark to visualize mitochondrial superoxide. The inspection was performed using a fluorescence microscope (BZ-9000; Keyence, Osaka, Japan) and a confocal microscope (FLUOVIEW FV10i; Olympus, Tokyo, Japan)

Rhodamine-phalloidin, MitoBright Green and JC-1 staining in cardiomyocytes

Rhodamine-phalloidin staining was performed to visualize F-actin within cardiomyocytes. Cells were stained with rhodamine-phalloidin (Thermo Fisher Scientific) and DAPI (Thermo Fisher Scientific) for 20 min at room temperature in

304 the dark. Mitochondrial activity was assessed using MitoBright Green staining
305 (Dojindo Molecular Technologies, Tokyo, Japan) according to the manufacturer's
306 protocol. Cells were stained with MitoBright Green and Hoechst 3334 for 30 min at
307 37˚C in the dark to visualize viable mitochondria. Mitochondrial membrane potential
308 was assessed using JC-1 staining (Dojindo Molecular Technologies) according to the
309 manufacturer's protocol. Cells were stained with JC-1 for 45 min at 37˚C in the dark.
310 JC-1 dye exhibits potential-dependent accumulation within mitochondria, indicated
311 by a fluorescence emission shift from green (~529 nm) to red (~590 nm).
312 Consequently, mitochondrial depolarization is indicated by a decrease in the red/green
313 fluorescence intensity ratio.
314
315 **Western blot analysis**
316 Neonatal cardiomyocytes were lysed by sonication in an ice-cold RIPA Lysis
317 Buffer System, which included protease inhibitors (Santa Cruz Biotechnology, Santa
318 Cruz, CA) and was supplemented with PhosSTOP phosphatase inhibitor (Roche
319 Applied Science, Upper Bavaria, Germany). Samples of the resultant lysate (1
320 μg/well) were subjected to electrophoresis using TGX gel (Bio-Rad Laboratories,
321 Hercules, CA), and the resolved proteins were transferred to PVDF membranes (Bio-
322 Rad Laboratories). After blocking in 5% skim milk, the membranes were incubated
323 with primary antibodies against CREB (Cat# ab31387, Abcam, Cambridge, England,
324 RRID:AB_731731) (32) at 1:1000 dilution and phospho-CREB (Cat# ab32096,
325 Abcam, RRID:AB_731734) (33) at 1:500 dilution, followed by a secondary antibody
326 (Cat# ab6721, Abcam, RRID:AB_955447) (34) at 1:3000 dilution. The bound
327 antibodies were visualized using chemiluminescent HRP substrate (Merck Millipore,
328 Burlington, MA), and the chemiluminescence was analyzed using an Image Quant
329 LAS 4000 system (GE Healthcare). Levels of CREB activation were determined
330 based on the ratio of band intensities after blotting with antibodies specific for the

phosphorylated and unphosphorylated proteins. For quantification, Western blot images were captured and analyzed using Image Quant TL software (GE Healthcare).

Measurement of mitochondrial oxygen consumption rate

An XFp Extracellular Flux Analyzer (Agilent, Santa Clara, CA) was used to record the oxygen consumption rate (OCR) as described previously (35). Primary neonatal cardiomyocytes were isolated and cultured in Agilent Seahorse cell culture miniplates. Two wells per plate did not contain cardiomyocytes and served as "background correction" wells. Oligomycin (2 μM) was added to cells, and the values were measured to calculate ATP-related OCR. FCCP [Carbonyl cyanide 4-(trifluoromethoxy) phenylhydrazone] (2 μM) and antimycin (1 μM) were added to cells, and the values were measured to calculate maximal and non-mitochondrial OCR, respectively. All OCR values were normalized by protein measurement.

Statistics

Statistical analysis was performed with GraphPad Prism software version 7.03. (GraphPad Software Inc., San Diego, CA). Quantitative values are expressed as the mean ± SEM. Significance of differences were assessed using Student's t test or two-way ANOVA with Tukey's test. Values of $p<0.05$ were considered significant.

"*" represents compared between the groups, "#" represents compared with wild-type mice SHAM, "†" represents compared with knockout mice SHAM. *, #, † represent $p<0.05$, **, ##, †† represent $p<0.01$ and ***, ###, ††† represent $p<0.001$.

Results

TAC-induced changes in heart weight and cardiac function in C-RAMP2-/- and RAMP3-/- mice

We previously generated and reported drug inducible, cardiomyocyte-specific RAMP2 KO mice (DI-C-RAMP2-/-) (36). In DI-C-RAMP2-/- mice, the spontaneous appearance of dilated cardiomyopathy-like heart failure was characteristically observed after the induction of the gene deletion. In the present study, therefore, we used a KO mouse line in which RAMP2 gene was congenitally deleted in a cardiomyocyte-specific manner (C-RAMP2-/-). Unlike DI-C-RAMP2-/-, C-RAMP2-/- mice were apparently normal. To evaluate the effect of RAMP2 deletion on the response to cardiovascular stress, we subjected C-RAMP2-/- mice to TAC. Although the hearts of C-RAMP2-/- mice exhibited no morphological abnormality under basal conditions, they rapidly developed hypertrophy after the TAC operation. In C-RAMP2-/- mice, heart weight/body weight (HW/BW) ratios and heart weight/tibia length (HW/TL) ratios were already significantly elevated after 1 week of TAC, as compared with their wild-type littermates (Figure 1A, B). On the other hand, RAMP3-/- mice showed no significant changes in HW/BW or HW/TL after TAC (Figure 1C, D).

In accordance with the morphological changes, echocardiography showed that within 1 week after TAC, C-RAMP2-/- mice developed cardiac dysfunction with significant decreases in ejection fraction (EF) and functional shortening (FS) as compared with their wild-type littermates (Figure 2A, B). On the other hand, in RAMP3-/- mice, the decrease of FS only became significant after 4 weeks of TAC (Figure 2C, D). In C-RAMP2-/- mice, significant LV dilatation (increased diastolic LV dimension; LVID;d) was observed at 4 weeks. In RAMP3-/-, by contrast, these changes were not significant.

In the hemodynamic analysis, we found that the maximum rate of rise in ventricular pressure (dP/dtmax) did not differ between C-RAMP2-/- mice and their

controls at baseline. However, dP/dtmax was significantly reduced in C-RAMP2-/- mice after 1 week of TAC. Similarly, the peak rate of pressure fall (dP/dtmin) was significantly reduced in C-RAMP2-/- mice after TAC (Figure 3A). By contrast, there were no significant changes in RAMP3-/- as compared to control mice (Figure 3B). These data indicate that reductions in ventricular contractility and relaxation are seen after TAC only in C-RAMP2-/- mice. Mean aortic pressure was not different in both C-RAMP2-/- and RAMP3-/- as compared with their wild-type littermates.

These observations suggest that, unlike in DI-C-RAMP2-/-, cardiac function is compensated under basal conditions in C-RAMP2-/- mice, but it is rapidly disrupted by induction of cardiac stress (1 week of TAC). This phenotype is much milder in RAMP3-/- mice, which only showed cardiac dysfunction after a more prolonged period of stress (4 weeks of TAC).

TAC-induced histological changes in the hearts of C-RAMP2-/- and RAMP3-/- mice

We next performed a histological analysis. Compared to their wild-type littermates, C-RAMP2-/- mice showed significant cardiomyocyte enlargement as early as 1 week after TAC (Figure 4A, B). Cardiac fibrosis is another important manifestation of the TAC model. Masson-trichrome staining revealed that both C-RAMP2-/- and RAMP3-/- hearts showed significant time-dependent increases in fibrotic area after TAC (Figure 5A-D). Interestingly, RAMP3-/- hearts showed prominent perivascular fibrosis after 4 weeks of TAC (Figure 5C, lower right panel). TAC is also associated by a reduction in cardiac capillary vessel density, which is indicative of maladaptation of vascular development during the cardiomyocyte hypertrophy (37). In C-RAMP2-/- hearts, the reduction in capillary density was significant after only 1 week of TAC, suggesting the maladaptive effects of the phenotype became apparent early in C-RAMP2-/- (Supplementary Figure 2) (24).

Next, the effect of TAC on the incidence of apoptosis within C-RAMP2-/- and RAMP3-/- hearts was evaluated using TUNEL. Interestingly, compared to hearts from their wild-type littermates, numbers of apoptotic cells were significantly higher in C-RAMP2-/- hearts, even without TAC (SHAM) and were further increased after 1 and 4 weeks of TAC (Figure 6A, B). In RAMP3-/- hearts, significantly higher numbers of apoptotic cells were observed after 4 weeks of TAC (Figure 5D, E). We also assessed the expression of the pro-apoptotic gene *Bax* and anti-apoptotic gene *Bcl2* and calculated the *Bax/Bcl2* ratio, which reflects the susceptibility to apoptosis. Compared to hearts from their wild-type littermates, those from C-RAMP2-/- mice showed significantly increased *Bax/Bcl2* ratios after 1 week of TAC (Figure 6C), which indicates that hearts with cardiomyocytes lacking the RAMP2 gene are more prone to apoptosis.

TAC-induced changes in mitochondrial structure and mitochondria-related gene expression in C-RAMP2-/- hearts

Succinate dehydrogenase (SDH, also known as complex II in the mitochondrial respiratory chain) catalyzes the oxidation of succinate to fumerate. SDH-staining thus reflects overall mitochondrial function (38). In sections of C-RAMP2-/- hearts, we detected smaller SDH-positive areas than in sections from wild-type hearts after 1 week of TAC (Figure 7A, B). Again, the change only became apparent in RAMP3-/- hearts after 4 weeks of TAC (Figure 7C, D).

We further analyzed cardiac gene expression using quantitative real-time PCR analysis (Figure 8A-D). We first assessed cardiac expression of several heart failure-related genes in C-RAMP2-/- (Figure 8A) and RAMP3-/- (Figure 8B) mice. Both C-RAMP2-/- and RAMP3-/- mice showed significant upregulation of BNP after 4 weeks of TAC. Assessment of mitochondria-related gene expression revealed that expression of PGC-1α and ATP synthase was significantly downregulated in C-RAMP2-/- (Figure 8C) but not RAMP3-/- mice (Figure 8D).

Electron microscopic observations revealed that, even without TAC, C-RAMP2-/- cardiomyocytes exhibited myofibrillar disarray and various mitochondrial structural abnormalities (dropout, swelling, deformation of cristae, and so on) (Figure 9A). TAC exacerbated the mitochondrial deformities in C-RAMP2-/- cardiomyocytes. No such changes were detected in RAMP3-/- cardiomyocytes (Figure 9B). These observations suggest that structural and functional abnormalities in cardiac mitochondria may explain the early onset of heart failure in C-RAMP2-/- mice under cardiovascular stress.

Abnormalities in primary cultured cardiomyocytes from C-RAMP2-/- mice

Given that C-RAMP2-/- mice rapidly developed cardiac dysfunction under conditions inducing cardiovascular stress, we next analyzed primary cardiomyocytes isolated from C-RAMP2-/- mice. We first confirmed that RAMP2 gene expression was reduced to about 20% of the wild-type level in the isolated cardiomyocytes (Supplementary Figure 3) (24). Using a Ca^{2+} imaging system to analyze twitch Ca^{2+} transients in Fluo-4-loaded cardiomyocytes, we found that the peak Ca^{2+} response ($\Delta F/F0$) – i.e., ratio of the peak cytosolic Ca^{2+} fluorescence elicited by electric pacing (ΔF) to the basal cytosol Ca^{2+} fluorescence without stimulation (F0) – was significantly lower in C-RAMP2-/- than wild-type cardiomyocytes (Supplementary Figure 4) (24). The observation suggests the presence of dysfunction in C-RAMP2-/- cardiomyocytes.

Using primary cultured cardiomyocytes isolated from C-RAMP2-/- mice, we also assessed the response to the β-receptor agonist ISO (10 μM, 24 h). In the presence of ISO, both dihydroethidium (DHE) staining (superoxide indicator of cytoplasm) (Figure 10A, B) and MitoSOX™ Red staining (superoxide indicator of mitochondria) (Figure 10C, D) were significantly enhanced in C-RAMP2-/- compared to wild-type cardiomyocytes. These results indicate that oxidative stress was elevated

in C-RAMP2-/- cardiomyocytes. On the other hand, no change in the oxidative stress level was detected in RAMP3-/- cardiomyocytes (Supplementary Figure 5) (24).

Treatment with ISO also significantly enhanced enlargement of C-RAMP2-/- cardiomyocytes as compared to the wild-type cells (Figure 11A). MitoBright green staining showed that the distribution of viable mitochondria was significantly reduced by ISO in C-RAMP2-/- cardiomyocytes (Figure 11B). At the same time, ISO significantly reduced the JC-1 red/green ratio in C-RAMP2-/- cardiomyocytes, indicating a marked reduction of mitochondrial membrane potential not seen in wild-type cells (Figure 11C). Contrary to these abnormalities found in C-RAMP2-/-, cardiomyocytes isolated from RAMP3-/- did not show apparent changes in mitochondria compared with wild-type (Supplementary Figure 6) (24).

In C-RAMP2-/- cardiomyocytes, ISO downregulated the expression of PGC-1α and PGC-1β (Figure 11D), two master regulators of mitochondrial biogenesis. Western blot analysis showed that the level of cAMP response element binding (CREB) protein activation is reduced in C-RAMP2-/- cardiomyocytes (Figure 11E). As CREB is known to upregulate expression of PGC-1α and PGC-1β (39), downregulation of CREB activation may underlie the observed cardiac mitochondrial dysfunction and heart failure in C-RAMP2-/- mice. In addition, mitochondrial respiration analysis (Mito stress test) showed that although maximal respiration and spare respiratory capacity were somewhat reduced in cultured neonatal C-RAMP2-/- cardiomyocytes, ATP production was unaffected under basal conditions (Supplementary Figure 7A, B) (24). In the presence of ISO, however, both mitochondrial respiration capacity and ATP production were lower in C-RAMP2-/- than wild-type cells (Supplementary Figure 7C, D) (24). These results indicate that the absence of RAMP2 clearly leads to mitochondrial dysfunction.

TAC-induced reduction of lymphatic vessels in RAMP3-/- mice

Given the marked changes in cardiac structure and function induced by TAC in C-RAMP2-/- mice, the effects of TAC in RAMP3-/- mice were comparatively mild. In fact, we detected no changes in cardiac mitochondria in RAMP3-/- mice. Still, after 4 weeks of TAC, there was a significant reduction in cardiac function with enhanced fibrosis in RAMP3-/- mice, as compared to their wild-type littermates. In an earlier study, we found that RAMP3-/- mice exhibited delayed drainage of lymphatic vessels, though the magnitude of the effect was subclinical (22). However, in a postoperative lymphedema model, RAMP3-/- mice exhibited greater edema with less lymphangiogenesis than wild-type mice (22). To clarify the mechanism for the milder and slower response to TAC in RAMP3-/- mice, we focused on the lymphatic vessels in the heart. To visualize cardiac lymphatic vessels, we immunostained sections of RAMP3-/- heart for lymphatic vessel marker LYVE-1. The staining revealed a significantly greater reduction of cardiac lymphatic vessels after 4 weeks of TAC in RAMP3-/- than wild-type mice (Figure 12A, B). AM was previously reported to regulate the expression of gap junction protein connexin 43 (Cx43) in lymphatic endothelial cells and promotes cardiac lymphangiogenesis (40,41). Therefore, we next analyzed Cx43 distribution in the heart sections, and found that Cx43-immunostaining was reduced in the TAC-operated RAMP3-/- compared to wild-type mice (Figure 13A, B). By contrast, lymphatic vessel density and Cx43 expression were unchanged in C-RAMP2-/- hearts (Supplementary Figure 8, 9) (24).

The lymphatic vasculature is essential for regulating tissue fluid homeostasis, and impairment of cardiac lymphatic drainage will likely lead to impair cardiac function. We therefore suggest that the reduction in lymphatic vessels in RAMP3-/- hearts could explain, at least in part, the RAMP3-/- phenotypes seen after 4 weeks of TAC.

519 **Discussion**

520 AM is now recognized to be a pleiotropic molecule involved in various diseases
521 (19). We and other groups have shown that AM's functions are regulated by its
522 receptor activity-modifying proteins, RAMPs (19). In particular, the combination of
523 CLR with RAMP2 or RAMP3 has a high affinity for AM (19). Although both
524 RAMP2 and RAMP3 are highly expressed in the heart from embryo to adulthood, the
525 functional differences between them had not been defined.

526 Among conventional RAMP KO mice, only conventional RAMP2-/- is
527 embryonically lethal (20). We previously reported on the cardiac effects of RAMP2
528 deletion using drug-inducible cardiomyocyte-specific RAMP2-/- (RAMP2 flox/flox-
529 αMHC-MerCreMer Tg mice; DI-C-RAMP2-/-) mice. In that study, acute deletion of
530 RAMP2 from adult hearts was achieved by treating the mice with tamoxifen (36). The
531 acute deletion of cardiac RAMP2 spontaneously evoked dilated cardiomyopathy-like
532 changes, clearly demonstrating that the AM-RAMP2 system is essential for
533 maintaining proper cardiac function. However, the rapid progression of the heart
534 failure and low survival rate made it difficult to analyze the role of the AM-RAMP2
535 system in chronic diseases. We also wondered whether the DI-C-RAMP2-/-
536 phenotypes may represent a state of decompensation due to the rapid loss of a specific
537 gene constitutively expressed in the heart. As hypertension is the most prevalent risk
538 factor for heart failure and plays a key role in its development (42), we were
539 interested in the impact of the RAMP2-/- and RAMP3-/- phenotypes in mice
540 experiencing pressure overload. In the present study, therefore, we applied the TAC
541 model to congenitally gene-deleted RAMP2 (C-RAMP2-/-) and RAMP3-/- mice to
542 evaluate the pathophysiological functions of the AM-RAMP2 and AM-RAMP3
543 systems during cardiovascular stress. C-RAMP2-/- and RAMP3-/- mice used in the
544 present study were apparently normal, and no significant changes in the heart were
545 observed under basal conditions. This suggests that, unlike in DI-C-RAMP2-/- mice,
546 cardiac function is compensated in C-RAMP2-/- mice. We speculated that in contrast

547 to acute gene deletion, congenital and chronic gene deletion may evoke adaptive
548 responses in the heart, and our gene expression analysis supports that idea. For
549 example, we observed that DI-C-RAMP2-/- mice exhibited upregulation of BNP, but
550 such changes were not observed in C-RAMP2-/- mice under basal conditions.
551 On the other hand, C-RAMP2-/- mice developed significant cardiac
552 hypertrophy and cardiac dysfunction within 1 week after TAC. This suggests that,
553 although cardiac function was compensated under basal conditions, decompensation
554 rapidly became developed under conditions of cardiovascular stress. RAMP3-/- also
555 showed reduced systolic function, but the dysfunction developed more slowly and did
556 not become significant until 4 weeks after TAC. This difference in the time course of
557 cardiac dysfunction in C-RAMP2-/- and RAMP3-/- mice is suggestive of the different
558 pathophysiological functions of the AM-RAMP2 and AM-RAMP3 systems in the
559 heart.
560 To shed light on the mechanism underlying the early maladaptation in C-
561 RAMP2-/- mice, we focused on the cardiac mitochondria. Even without TAC-
562 treatment, electron microscopic examination revealed mitochondrial abnormalities in
563 C-RAMP2-/- hearts. We therefore speculated that cardiac mitochondrial abnormalities
564 may explain the early onset of heart failure in C-RAMP2-/- mice subjected to
565 cardiovascular stress. To further confirm that mitochondrial dysfunction is the
566 primary cause of heart failure, and is not secondary to the contractile dysfunction, we
567 cultured primary cardiomyocytes isolated from C-RAMP2-/- hearts. ISO induced
568 marked changes in mitochondria in neonatal cardiomyocytes from C-RAMP2-/-
569 hearts. It reduced the number of viable mitochondria, reduced mitochondrial
570 membrane potential, and enhanced mitochondria-derived superoxide production. In
571 addition, cardiomyocytes from C-RAMP2-/- hearts showed downregulation of the
572 transcriptional coactivators PGC-1α and PGC-1β, which govern mitochondrial
573 biology through broad regulation of genes in both the nuclear and mitochondrial
574 genomes (43). We also found that CREB activation was reduced in C-RAMP2-/-

575 cardiomyocytes. As CREB regulates PGC-1α and PGC-1β gene expression by
576 binding to the cAMP responsive element in their promoter regions (39), we suggest
577 that CREB suppression underlies the observed mitochondrial dysfunction and heart
578 failure in C-RAMP2-/- mice. Downstream effects mediated by the AM-RAMP2
579 system include cAMP production, Ca^{2+} mobilization (44) and activation of Akt and
580 other signaling molecules (45). All of these effectors are involved in CREB activation
581 (46-48), which suggests RAMP2 deletion suppresses CREB activation by altering
582 several signaling pathways, which in turn leads to downregulation of PGC-1α and
583 PGC-1β.
584 In contrast to C-RAMP2-/- mice, no abnormalities of cardiac mitochondria
585 were seen in RAMP3-/- mice. Using lymphangiography, we previously found that
586 drainage of subcutaneous lymphatic vessels was delayed in RAMP3-/- mice (22). In a
587 post-operative lymphedema model, RAMP3-/- mice showed more severe interstitial
588 edema than wild-type mice, with fewer lymphatic vessels and accumulation of
589 inflammatory cells (22). Recently, Trincot et al. reported that AM enhances
590 lymphangiogenesis in the heart after ischemic injury and prevents remodeling and
591 cardiac dysfunction (41). They also reported that AM increases the expression of
592 Cx43 and gap junction formation in the lymphatic endothelial cells, which is involved
593 in the proper contraction of the cardiac lymphatic vessels as well as
594 lymphangiogenesis. We therefore assessed the changes in lymphatic vessels within
595 the hearts after TAC and found that lymphatic vessel density was significantly lower
596 in RAMP3-/- than wild-type mice after TAC. Furthermore, we found that Cx43
597 expression in the heart was reduced in RAMP3-/- after TAC. These observations
598 suggest that Cx43 expression and lymphangiogenesis induced by AM in the previous
599 study can be explained mainly by RAMP3. AM reportedly exerts anti-apoptotic
600 effects mediated via the PI3K-Akt pathway (49). We previously observed that, among
601 the RAMP subisoforms, RAMP3 is the most highly expressed in lymphatic
602 endothelial cells (22). We also found that primary lymphatic endothelial cells cultured

603 from RAMP3-/- mice showed weaker PI3K-Akt activation in response to AM (22).
604 We therefore suggest the AM-RAMP3 system is essential for appropriate regulation
605 of lymphangiogenesis and that it acts via the PI3K-Akt pathway in lymphatic
606 endothelial cells. Lymphatic vessels play a key role in regulating tissue fluid
607 homeostasis to maintain interstitial fluid equilibrium in the heart and normal cardiac
608 function, and to prevent remodeling of the injured heart (50). Reducing lymphatic
609 vessels increases myocardial interstitial edema, which in turn increases ventricular
610 stiffness and decreases cardiac performance (51,52). We therefore speculate that the
611 later manifestation of abnormalities in RAMP3-/- mice may be explained, at least in
612 part, by a reduction in lymphatic vessels.
613 In the present study, both C-RAMP2-/- and RAMP3-/- mice showed more
614 severe fibrosis than their wild-type littermates. In C-RAMP2-/- mice, the worsening
615 of cardiac fibrosis is to be expected, as enhancement of cardiac hypertrophy is
616 associated with activation of profibrotic genetic pathways (53). By contrast, the
617 enhanced cardiac fibrosis observed in RAMP3-/- mice was independent of cardiac
618 hypertrophy. Instead, we focused on the characteristic perivascular fibrosis observed
619 in RAMP3-/- hearts after TAC. We speculate that reduced lymphangiogenesis in the
620 perivascular region of RAMP3-/- hearts would result in excess fluid and lymphatic
621 cells within the myocardial interstitial space, which would in turn exacerbate cardiac
622 inflammation and fibrosis (51,54). In RAMP3-/- hearts, however, the alterations in
623 fibrosis and lymphatic vessels were detected in parallel, so it is also possible that the
624 fibrosis could be the cause of the observed lymphatic abnormality.
625 Limitation of the present study is that, while using conventional RAMP3-/-, we
626 used cardiomyocyte-specific RAMP2-/-, because of the embryonic lethality of
627 conventional RAMP2-/-. Therefore, we had to evaluate phenotypes of each KO line
628 only in comparison with each wild-type littermate. However, phenotypes of
629 conventional KO are expected to be more severe than those of cell-specific KO.
630 Nevertheless, conventional RAMP3-/- showed much milder phenotype than

cardiomyocyte-specific RAMP2-/- in this study, suggesting that RAMP2 is more essential for cardiomyocyte function. In our preliminary TAC study using cardiomyocyte-specific RAMP3-/-, we have not found apparent cardiac dysfunction compared with their wild-type littermate so far.

Figure 14 summarizes our findings of the pathophysiological roles of the AM-RAMP2 and AM-RAMP3 systems under conditions of cardiovascular stress. The AM-RAMP2 system regulates cardiac mitochondrial homeostasis by regulating CREB-PGC1 pathway and is necessary for earlier stage adaptation, while the AM-RAMP3 system is necessary at later stage adaptation through regulation of Cx43 expression and lymphatic vessel homeostasis. Thus, both the AM-RAMP2 and AM-RAMP3 systems play critical roles in the maintenance of cardiac homeostasis in the face of cardiovascular stress.

Plasma AM levels are increased in patients with heart failure (12,13). Cardiac levels of AM, RAMP2 and RAMP3 are also reportedly increased in failing hearts (55,56). Nagaya et al. reported that intravenous infusion of human AM has beneficial effects in patients with heart failure (57). AM infusion markedly increases the cardiac index and decreases pulmonary capillary wedge pressure. This suggests the increases in AM, RAMP2 and RAMP3 seen in heart failure may work as a compensatory adaptation. Given these observations, the clinical application of AM is much anticipated. Unfortunately, vasoactive peptides like AM have a short half-life in the bloodstream, which limits their usefulness in the treatment of chronic diseases. It is therefore noteworthy if we could modulate the function of AM by modulating RAMPs. In that context, RAMP2 and RAMP3 could be promising alternative therapeutic targets for the treatment of heart failure.

Figure Legends

Figure 1

Changes of the heart weight after TAC

A, C: Hematoxylin and eosin stained transverse heart sections from C-RAMP2-/- (**A**) and RAMP3-/- (**C**) mice and their wild-type littermates after 1 week of TAC. Scale bars = 200 μm. **B, D:** Heart weight / body weight (HW/BW) and heart weight / tibialis length (HW/TL) ratios in C-RAMP2-/- (**B**) and RAMP3-/- (**D**) mice and their wild-type littermates. Data are expressed as means ± SEM. n = 10 in C-RAMP2-/- and C-RAMP2+/+; n = 8 in RAMP3-/- and RAMP3+/+. "*" represents compared between the groups, "#" represents compared with wild-type mice SHAM, "†" represents compared with knockout mice SHAM (Two-way ANOVA with Tukey's test).

Figure 2

Changes of cardiac function and morphology after TAC

A-D: Results of echocardiography after TAC in C-RAMP2-/- (**A, B**) and RAMP3-/- (**C, D**) mice and their wild-type littermates. **A, C:** Representative transthoracic M-mode echocardiograms. **B, D:** Measurements of ejection fraction (EF), functional shortening (FS), diastolic interventricular septum (IVS;d), diastolic left ventricular dimension (LVID;d), and diastolic left ventricular posterior wall (LVPW;d). Data are expressed as means ± SEM. n = 10 in C-RAMP2-/- and C-RAMP2+/+; n = 8 in RAMP3-/- and RAMP3+/+. "*" represents compared between the groups, "#" represents compared with wild-type mice SHAM, "†" represents compared with knockout mice SHAM (Two-way ANOVA with Tukey's test).

Figure 3

Hemodynamic measurements

687 **A, B,** Maximum rate of rise in left ventricular pressure (dP/dt_{max}), peak rate of left
688 ventricular pressure fall (dP/dt_{min}), left ventricular end-diastolic pressure (LVEDP)
689 and mean aortic pressure were analyzed in C-RAMP2-/- (**A**) and RAMP3-/- (**B**) mice
690 and their controls. Data are expressed as means ± SEM. n = 5 in SHAM groups; n = 6
691 in C-RAMP2+/+ and C-RAMP2-/- TAC groups; n = 4 in RAMP3+/+ TAC group; n =
692 3 in RAMP3-/- TAC group. "*" represents compared between the groups (Student's t-
693 test).
694
695 **Figure 4**
696 **Cardiac hypertrophy caused by TAC**
697 **A, C:** Hematoxylin/eosin-stained heart sections from C-RAMP2-/- (**A**) and RAMP3-/-
698 (**C**) mice and their wild-type littermates (SHAM, TAC 1W, TAC 4W). Scale bars =
699 50 μm. **B, D:** Measurement of cardiomyocyte diameter in C-RAMP2-/- (**B**) and
700 RAMP3-/- (**D**) mice and their wild-type littermates. Data are expressed as means ±
701 SEM. n = 10 in C-RAMP2-/- and C-RAMP2+/+; n = 8 in RAMP3-/- and RAMP3+/+
702 "*" represents compared between the groups, "#" represents compared with wild-type
703 mice SHAM, "†" represents compared with knockout mice SHAM (Two-way
704 ANOVA with Tukey's test).
705
706 **Figure 5**
707 **Cardiac fibrosis caused by TAC**
708 **A, C:** Masson's trichrome-stained heart sections from C-RAMP2-/- (**A**) and
709 RAMP3-/- (**C**) mice and their wild-type littermates (SHAM, TAC 1W, TAC 4W).
710 Scale bars = 100 μm. **B, D:** Measurements of fibrotic area / field (x100) in
711 C-RAMP2-/- (**B**) and RAMP3-/- (**D**) mice and their wild-type littermates. Data are
712 expressed as means ± SEM. n = 11 in RAMP3-/- TAC 4W and n = 12 in other groups.
713 "*" represents compared between the groups, "#" represents compared with wild-type

714 mice SHAM, "†" represents compared with knockout mice SHAM (Two-way
715 ANOVA with Tukey's test).
716
717 **Figure 6**
718 **Appearance of apoptotic cells after TAC**
719 **A, D:** TUNEL in heart sections from C-RAMP2-/- (**A**) and RAMP3-/- (**D**) mice and
720 their wild-type littermates (SHAM, TAC 1W, TAC 4W). Scale bars = 100 μm. **B, E:**
721 Numbers of TUNEL-positive cells / field (x100) in heart sections from C-RAMP2-/-
722 (**B**) and RAMP3-/- (**E**) mice and their wild-type littermates. Data are expressed as
723 means ± SEM. n = 4 in each group. "*" represents compared between the groups, "#"
724 represents compared with wild-type mice SHAM, "†" represents compared with
725 knockout mice SHAM (Two-way ANOVA with Tukey's test). **C, F:** Real-time PCR
726 analysis of the Bax / Bcl-2 expression ratio in hearts from C-RAMP2-/- (**C**) and
727 RAMP3-/- (**F**) mice and their wild-type littermates. Mean Bax and Bcl-2 expression
728 in SHAM-operated wild-type mice was assigned a value of 1, and the Bax / Bcl-2
729 ratio was calculated. Data are expressed as means ± SEM. n = 5 in each group. "*"
730 represents compared between the groups, "#" represents compared with wild-type
731 mice SHAM, "†" represents compared with knockout mice SHAM (Two-way
732 ANOVA with Tukey's test).
733
734 **Figure 7**
735 **Reduction of succinate dehydrogenase (SDH)-staining after TAC**
736 **A, C:** Succinate dehydrogenase (SDH) staining in heart sections from C-RAMP2-/-
737 (**B**) and RAMP3-/- (**C**) mice and their wild-type littermates (SHAM, TAC 1W, TAC
738 4W). Scale bars = 100 μm. **B, D:** SDH-positive area / field (x100) in heart sections
739 from C-RAMP2-/- (**B**) and RAMP3-/- (**D**) mice and their wild-type littermates. Data
740 are expressed as means ± SEM. n = 6 in C-RAMP2-/- and C-RAMP2+/+; n = 4 in
741 RAMP3-/- and RAMP3+/+. "*" represents compared between the groups, "#"

represents compared with wild-type mice SHAM, "†" represents compared with knockout mice SHAM (Two-way ANOVA with Tukey's test).

Figure 8

TAC-induced changes in gene expression in the heart

A-D: Real-time PCR analysis of mRNA expression of heart failure-related genes (**A, B**) and mitochondria-related genes (**C, D**) in C-RAMP2-/- (**A, C**) and RAMP3-/- (**B, D**) mice and their wild-type littermates (SHAM, TAC 1W, TAC 4W). Means in wild-type mice were assigned a value of 1. Data are expressed as means ± SEM. n = 5 in each group. "*" represents compared between the groups (Student's t-test).

Figure 9

Transmission electron microscopic analysis of cardiac mitochondria

A: In C-RAMP2-/- cardiomyocytes, myofibrillar disarray and irregularity of mitochondrial size and shape were observed, even in the sham group. TAC exacerbated the mitochondrial deformity. **B:** There were no apparent ultrastructural changes in RAMP3-/- cardiomyocytes compared with RAMP3+/+ cardiomyocytes. Scale bars = 1 μm.

Figure 10

Isoproterenol (ISO)-induced changes in oxidative stress in primary cultured neonatal cardiomyocytes from C-RAMP2-/-

Cardiomyocytes were isolated from P0 C-RAMP2-/- or wild-type neonates, cultured for 72 h and stimulated for 24 h with 10 μM ISO or control medium (CONT). **A, C:** Dihydroethidium (cytosolic superoxide indicator) staining (**A**) and MitoSOX™ Red (mitochondrial superoxide indicator) staining (**C**) in primary cultured cardiomyocytes. Scale bars = 100 μm. **B, D:** Dihydroethidium-positive (**B**) and MitoSOX™ Red-positive (**D**) areas (μm^2) / field (x100) in primary cultured cardiomyocytes. Data are

770 expressed as means ± SEM. n = 5 in each group. "*" represents compared between
771 the groups (Student's t-test).
772
773 **Figure 11**
774 **ISO-induced changes in mitochondrial function in primary cultured neonatal**
775 **cardiomyocytes from C-RAMP2-/-**
776 Cardiomyocytes were isolated from P0 C-RAMP2-/- or wild-type neonates, cultured
777 for 72 h and stimulated for 24 h with 10 μM ISO or control medium (CONT). **A:**
778 Phalloidin-stained cardiomyocytes showing actin filaments **(left)**. Cardiomyocyte
779 sizes were compared between C-RAMP2-/- and wild-type cells (**right**). **B:** MitoBright
780 Green-stained cardiomyocytes showing viable mitochondria **(left)**. MitoBright
781 Green-positive areas / field (x400) were compared between C-RAMP2-/- and wild-
782 type cells (**right**). **C**: JC-1-stained (mitochondrial membrane potential indicator)
783 cardiomyocytes **(left)**. Red / green fluorescence ratios were compared between
784 C-RAMP2-/- and wild-type cells (**right**). Mitochondrial depolarization is indicated by
785 a decrease in the red/green fluorescence intensity ratio. Scale bars in **A-C** are 10 μm.
786 Data are expressed as means ± SEM. n = 5 in each group**.** "*" represents compared
787 between the groups (Student's t-test). **D**: Real-time PCR analysis of the expression of
788 mitochondria-related genes in control (CONT) and ISO-treated neonatal
789 cardiomyocytes. The mean in wild-type cardiomyocytes was assigned a value of 1.
790 Data are expressed as means ± SEM. n = 5 in each group. "*" represents compared
791 between the groups (Student's t-test). **E,** Western blot analysis of CREB and
792 phosphorylated (activated) CREB (p-CREB) in primary cultured cardiomyocytes. The
793 level of CREB activation is indicated by the ratio of band intensity (p-CREB/CREB).
794 Data are expressed as means ± SEM. n = 5 in each group. "*" represents compared
795 between the groups (Student's t-test).
796

Figure 12

TAC-induced reduction of lymphatic vessel density in RAMP3-/- hearts

A: LYVE-1 and CD31-immunostained heart sections from RAMP3-/- mice and their wild-type littermates (SHAM, TAC 1W, TAC 4W). (green = LYVE-1, red = CD31). Scale bars = 100 μm. **B:** Comparison of the number of lymphatic vessels / field (x100) in heart sections from RAMP3-/- mice and their wild-type littermates. Data are expressed as means ± SEM. n = 4 in each group. "*" represents compared between the groups, "#" represents compared with wild-type mice SHAM, "†" represents compared with knockout mice SHAM (Two-way ANOVA with Tukey's test).

Figure 13

TAC-induced reduction of Cx43 localization in RAMP3-/- hearts

A: Cx43-immunostained heart sections from RAMP3-/- mice and their wild-type littermates (TAC 4W). (green = Cx43, red = WGA). Scale bars = 100 μm. **B:** Comparison of the Cx43-positve area (μm^2) / field (x 200) in heart sections from RAMP3-/- mice and their wild-type littermates. Data are expressed as means ± SEM. n =4 in each group. "*" represents compared between the groups (Student's t-test).

Figure 14

Pathophysiological roles of the AM-RAMP2 and AM-RAMP3 systems under conditions of cardiovascular stress

The AM-RAMP2 system regulates cardiac mitochondrial homeostasis and is necessary for earlier stage adaptation, while the AM-RAMP3 system is necessary at later stage adaptation through regulation of lymphatic vessel homeostasis. Thus, both the AM-RAMP2 and AM-RAMP3 systems play critical roles in the maintenance of cardiac homeostasis in the face of cardiovascular stress.

Acknowledgement

The authors are grateful to Dr. Motoaki Sano for valuable comments and αMHC-Cre transgenic mice.

Data availability statement

Some or all data generated or analyzed during this study are included in this published article or in the data repositories listed in References.

References

1. Virani SS, Alonso A, Benjamin EJ, Bittencourt MS, Callaway CW, Carson AP, Chamberlain AM, Chang AR, Cheng S, Delling FN, Djousse L, Elkind MSV, Ferguson JF, Fornage M, Khan SS, Kissela BM, Knutson KL, Kwan TW, Lackland DT, Lewis TT, Lichtman JH, Longenecker CT, Loop MS, Lutsey PL, Martin SS, Matsushita K, Moran AE, Mussolino ME, Perak AM, Rosamond WD, Roth GA, Sampson UKA, Satou GM, Schroeder EB, Shah SH, Shay CM, Spartano NL, Stokes A, Tirschwell DL, VanWagner LB, Tsao CW, American Heart Association Council on E, Prevention Statistics C, Stroke Statistics S. Heart Disease and Stroke Statistics-2020 Update: A Report From the American Heart Association. Circulation 2020; 141:e139-e596
2. Mendis S. Global progress in prevention of cardiovascular disease. Cardiovasc Diagn Ther 2017; 7:S32-S38
3. Grieco P, Gomez-Monterrey I. Natural and synthetic peptides in the cardiovascular diseases: An update on diagnostic and therapeutic potentials. Arch Biochem Biophys 2019; 662:15-32
4. Kitamura K, Kangawa K, Kawamoto M, Ichiki Y, Nakamura S, Matsuo H, Eto T. Adrenomedullin: a novel hypotensive peptide isolated from human pheochromocytoma. Biochem Biophys Res Commun 1993; 192:553-560
5. Ichiki Y, Kitamura K, Kangawa K, Kawamoto M, Matsuo H, Eto T. Distribution and characterization of immunoreactive adrenomedullin in human tissue and plasma. FEBS Lett 1994; 338:6-10
6. Michibata H, Mukoyama M, Tanaka I, Suga S, Nakagawa M, Ishibashi R, Goto M, Akaji K, Fujiwara Y, Kiso Y, Nakao K. Autocrine/paracrine role of adrenomedullin in cultured endothelial and mesangial cells. Kidney Int 1998; 53:979-985
7. Kitamura K, Ichiki Y, Tanaka M, Kawamoto M, Emura J, Sakakibara S, Kangawa K, Matsuo H, Eto T. Immunoreactive adrenomedullin in human plasma. FEBS Lett 1994; 341:288-290
8. Nishikimi T, Matsuoka H. Cardiac adrenomedullin: its role in cardiac hypertrophy and heart failure. Curr Med Chem Cardiovasc Hematol Agents 2005; 3:231-242
9. Jougasaki M, Wei CM, Aarhus LL, Heublein DM, Sandberg SM, Burnett JC, Jr. Renal localization and actions of adrenomedullin: a natriuretic peptide. Am J Physiol 1995; 268:F657-663
10. Shimosawa T, Shibagaki Y, Ishibashi K, Kitamura K, Kangawa K, Kato S, Ando K, Fujita T. Adrenomedullin, an endogenous peptide, counteracts cardiovascular damage. Circulation 2002; 105:106-111
11. Shimosawa T, Ogihara T, Matsui H, Asano T, Ando K, Fujita T. Deficiency of adrenomedullin induces insulin resistance by increasing oxidative stress. Hypertension 2003; 41:1080-1085
12. Nishikimi T, Saito Y, Kitamura K, Ishimitsu T, Eto T, Kangawa K, Matsuo H,

Omae T, Matsuoka H. Increased plasma levels of adrenomedullin in patients with heart failure. J Am Coll Cardiol 1995; 26:1424-1431

13. Jougasaki M, Wei CM, McKinley LJ, Burnett JC, Jr. Elevation of circulating and ventricular adrenomedullin in human congestive heart failure. Circulation 1995; 92:286-289.

14. Nagaya N, Nishikimi T, Yoshihara F, Horio T, Morimoto A, Kangawa K. Cardiac adrenomedullin gene expression and peptide accumulation after acute myocardial infarction in rats. Am J Physiol Regul Integr Comp Physiol 2000; 278:R1019-1026

15. Iimuro S, Shindo T, Moriyama N, Amaki T, Niu P, Takeda N, Iwata H, Zhang Y, Ebihara A, Nagai R. Angiogenic effects of adrenomedullin in ischemia and tumor growth. Circ Res 2004; 95:415-423

16. Shindo T, Kurihara Y, Nishimatsu H, Moriyama N, Kakoki M, Wang Y, Imai Y, Ebihara A, Kuwaki T, Ju KH, Minamino N, Kangawa K, Ishikawa T, Fukuda M, Akimoto Y, Kawakami H, Imai T, Morita H, Yazaki Y, Nagai R, Hirata Y, Kurihara H. Vascular abnormalities and elevated blood pressure in mice lacking adrenomedullin gene. Circulation 2001; 104:1964-1971

17. Nishimatsu H, Suzuki E, Nagata D, Moriyama N, Satonaka H, Walsh K, Sata M, Kangawa K, Matsuo H, Goto A, Kitamura T, Hirata Y. Adrenomedullin induces endothelium-dependent vasorelaxation via the phosphatidylinositol 3-kinase/Akt-dependent pathway in rat aorta. Circ Res 2001; 89:63-70

18. McLatchie LM, Fraser NJ, Main MJ, Wise A, Brown J, Thompson N, Solari R, Lee MG, Foord SM. RAMPs regulate the transport and ligand specificity of the calcitonin-receptor-like receptor. Nature 1998; 393:333-339

19. Shindo T, Tanaka M, Kamiyoshi A, Ichikawa-Shindo Y, Kawate H, Yamauchi A, Sakurai T. Regulation of cardiovascular development and homeostasis by the adrenomedullin-RAMP system. Peptides 2019; 111:55-61

20. Ichikawa-Shindo Y, Sakurai T, Kamiyoshi A, Kawate H, Iinuma N, Yoshizawa T, Koyama T, Fukuchi J, Iimuro S, Moriyama N, Kawakami H, Murata T, Kangawa K, Nagai R, Shindo T. The GPCR modulator protein RAMP2 is essential for angiogenesis and vascular integrity. J Clin Invest 2008; 118:29-39

21. Koyama T, Ochoa-Callejero L, Sakurai T, Kamiyoshi A, Ichikawa-Shindo Y, Iinuma N, Arai T, Yoshizawa T, Iesato Y, Lei Y, Uetake R, Okimura A, Yamauchi A, Tanaka M, Igarashi K, Toriyama Y, Kawate H, Adams RH, Kawakami H, Mochizuki N, Martinez A, Shindo T. Vascular endothelial adrenomedullin-RAMP2 system is essential for vascular integrity and organ homeostasis. Circulation 2013; 127:842-853

22. Yamauchi A, Sakurai T, Kamiyoshi A, Ichikawa-Shindo Y, Kawate H, Igarashi K, Toriyama Y, Tanaka M, Liu T, Xian X, Imai A, Zhai L, Owa S, Arai T, Shindo T. Functional differentiation of RAMP2 and RAMP3 in their regulation of the vascular system. J Mol Cell Cardiol 2014; 77:73-85

23. Gaussin V, Van de Putte T, Mishina Y, Hanks MC, Zwijsen A, Huylebroeck D,

Behringer RR, Schneider MD. Endocardial cushion and myocardial defects after cardiac myocyte-specific conditional deletion of the bone morphogenetic protein receptor ALK3. Proc Natl Acad Sci U S A 2002; 99:2878-2883

24. Shindo T. Data from: Adrenomedullin-RAMP2 and -RAMP3 systems regulate cardiac homeostasis during cardiovascular stress. Dryad Digital Repository. https://datadryad.org/stash/share/U401M43tEwTli_HKzCPF5tt5oGqyie-gVLt71f-F060. .

25. deAlmeida AC, van Oort RJ, Wehrens XH. Transverse aortic constriction in mice. J Vis Exp 2010; 38:1729

26. Rockman HA, Ross RS, Harris AN, Knowlton KU, Steinhelper ME, Field LJ, Ross J, Jr., Chien KR. Segregation of atrial-specific and inducible expression of an atrial natriuretic factor transgene in an in vivo murine model of cardiac hypertrophy. Proc Natl Acad Sci U S A 1991; 88:8277-8281

27. RRID:AB_2783787. https://scicrunch.org/resolver/RRID:AB_2783787

28. RRID:AB_396660. https://scicrunch.org/resolver/RRID:AB_396660

29. RRID:AB_476857. https://scicrunch.org/resolver/RRID:AB_476857

30. Ackers-Johnson M, Li PY, Holmes AP, O'Brien SM, Pavlovic D, Foo RS. A Simplified, Langendorff-Free Method for Concomitant Isolation of Viable Cardiac Myocytes and Nonmyocytes From the Adult Mouse Heart. Circ Res 2016; 119:909-920

31. Nakada T, Flucher BE, Kashihara T, Sheng X, Shibazaki T, Horiuchi-Hirose M, Gomi S, Hirose M, Yamada M. The proximal C-terminus of alpha(1C) subunits is necessary for junctional membrane targeting of cardiac L-type calcium channels. Biochem J 2012; 448:221-231

32. RRID:AB_731731. https://scicrunch.org/resolver/RRID:AB_731731

33. RRID:AB_731734. https://scicrunch.org/resolver/RRID:AB_731734

34. RRID:AB_955447. https://scicrunch.org/resolver/RRID:AB_955447

35. Ding M, Liu C, Shi R, Yu M, Zeng K, Kang J, Fu F, Mi M. Mitochondrial fusion promoter restores mitochondrial dynamics balance and ameliorates diabetic cardiomyopathy in an optic atrophy 1-dependent way. Acta Physiol (Oxf) 2020; 229:e13428

36. Yoshizawa T, Sakurai T, Kamiyoshi A, Ichikawa-Shindo Y, Kawate H, Iesato Y, Koyama T, Uetake R, Yang L, Yamauchi A, Tanaka M, Toriyama Y, Igarashi K, Nakada T, Kashihara T, Yamada M, Kawakami H, Nakanishi H, Taguchi R, Nakanishi T, Akazawa H, Shindo T. Novel regulation of cardiac metabolism and homeostasis by the adrenomedullin-receptor activity-modifying protein 2 system. Hypertension 2013; 61:341-351

37. Sano M, Minamino T, Toko H, Miyauchi H, Orimo M, Qin Y, Akazawa H, Tateno K, Kayama Y, Harada M, Shimizu I, Asahara T, Hamada H, Tomita S, Molkentin JD, Zou Y, Komuro I. p53-induced inhibition of Hif-1 causes cardiac dysfunction during pressure overload. Nature 2007; 446:444-448

38. Wust RC, Myers DS, Stones R, Benoist D, Robinson PA, Boyle JP, Peers C,

White E, Rossiter HB. Regional skeletal muscle remodeling and mitochondrial dysfunction in right ventricular heart failure. Am J Physiol Heart Circ Physiol 2012; 302:H402-411

39. Herzig S, Long F, Jhala US, Hedrick S, Quinn R, Bauer A, Rudolph D, Schutz G, Yoon C, Puigserver P, Spiegelman B, Montminy M. CREB regulates hepatic gluconeogenesis through the coactivator PGC-1. Nature 2001; 413:179-183

40. Karpinich NO, Caron KM. Gap junction coupling is required for tumor cell migration through lymphatic endothelium. Arterioscler Thromb Vasc Biol 2015; 35:1147-1155

41. Trincot CE, Xu W, Zhang H, Kulikauskas MR, Caranasos TG, Jensen BC, Sabine A, Petrova TV, Caron KM. Adrenomedullin Induces Cardiac Lymphangiogenesis After Myocardial Infarction and Regulates Cardiac Edema Via Connexin 43. Circ Res 2019; 124:101-113

42. Teo LY, Chan LL, Lam CS. Heart failure with preserved ejection fraction in hypertension. Curr Opin Cardiol 2016; 31:410-416

43. Jones AW, Yao Z, Vicencio JM, Karkucinska-Wieckowska A, Szabadkai G. PGC-1 family coactivators and cell fate: roles in cancer, neurodegeneration, cardiovascular disease and retrograde mitochondria-nucleus signalling. Mitochondrion 2012; 12:86-99

44. Shimekake Y, Nagata K, Ohta S, Kambayashi Y, Teraoka H, Kitamura K, Eto T, Kangawa K, Matsuo H. Adrenomedullin stimulates two signal transduction pathways, cAMP accumulation and Ca2+ mobilization, in bovine aortic endothelial cells. J Biol Chem 1995; 270:4412-4417.

45. Yanagawa B, Nagaya N. Adrenomedullin: molecular mechanisms and its role in cardiac disease. Amino Acids 2007; 32:157-164

46. Du K, Montminy M. CREB is a regulatory target for the protein kinase Akt/PKB. J Biol Chem 1998; 273:32377-32379

47. Sheng M, Thompson MA, Greenberg ME. CREB: a Ca(2+)-regulated transcription factor phosphorylated by calmodulin-dependent kinases. Science 1991; 252:1427-1430

48. Gonzalez GA, Montminy MR. Cyclic AMP stimulates somatostatin gene transcription by phosphorylation of CREB at serine 133. Cell 1989; 59:675-680

49. Miyashita K, Itoh H, Sawada N, Fukunaga Y, Sone M, Yamahara K, Yurugi-Kobayashi T, Park K, Nakao K. Adrenomedullin provokes endothelial Akt activation and promotes vascular regeneration both in vitro and in vivo. FEBS Lett 2003; 544:86-92

50. Flaht-Zabost A, Gula G, Ciszek B, Czarnowska E, Jankowska-Steifer E, Madej M, Niderla-Bielinska J, Radomska-Lesniewska D, Ratajska A. Cardiac mouse lymphatics: developmental and anatomical update. Anat Rec (Hoboken) 2014; 297:1115-1130

51. Laine GA, Allen SJ. Left ventricular myocardial edema. Lymph flow, interstitial fibrosis, and cardiac function. Circ Res 1991; 68:1713-1721

52. Pogatsa G, Dubecz E, Gabor G. The role of myocardial edema in the left ventricular diastolic stiffness. Basic Res Cardiol 1976; 71:263-269
53. Ho CY, Lopez B, Coelho-Filho OR, Lakdawala NK, Cirino AL, Jarolim P, Kwong R, Gonzalez A, Colan SD, Seidman JG, Diez J, Seidman CE. Myocardial fibrosis as an early manifestation of hypertrophic cardiomyopathy. N Engl J Med 2010; 363:552-563
54. Huang LH, Lavine KJ, Randolph GJ. Cardiac Lymphatic Vessels, Transport, and Healing of the Infarcted Heart. JACC Basic Transl Sci 2017; 2:477-483
55. Totsune K, Takahashi K, Mackenzie HS, Murakami O, Arihara Z, Sone M, Mouri T, Brenner BM, Ito S. Increased gene expression of adrenomedullin and adrenomedullin-receptor complexes, receptor-activity modifying protein (RAMP)2 and calcitonin-receptor-like receptor (CRLR) in the hearts of rats with congestive heart failure. Clin Sci (Lond) 2000; 99:541-546
56. Oie E, Ahmed MS, Ueland T, Sikkeland LI, Dahl CP, Hagelin EM, von Lueder T, Edvardsen T, Andreassen AK, Gullestad L, Aukrust P, Yndestad A, Vinge LE, Attramadal H. Adrenomedullin is increased in alveolar macrophages and released from the lungs into the circulation in severe heart failure. Basic Res Cardiol 2010; 105:89-98
57. Nagaya N, Satoh T, Nishikimi T, Uematsu M, Furuichi S, Sakamaki F, Oya H, Kyotani S, Nakanishi N, Goto Y, Masuda Y, Miyatake K, Kangawa K. Hemodynamic, renal, and hormonal effects of adrenomedullin infusion in patients with congestive heart failure. Circulation 2000; 101:498-503.

Table 1 Primers and probes used for real-time PCR

Adm (adrenomedullin)	Forward	5'-GGACACTGCAGGGCCAGAT-3'
	Reverse	5'-GTAGTTCCCTCTTCCCACGACTTA-3'
Ramp2	Probe	5'-CCCAGAGGATGTGCTCCTGGCCAT-3'
	Forward	5'-GCAGCCCACCTTCTCTGATC-3'
	Reverse	5'-AACGGGATGAGGCAGATGG-3'
Ramp3	Forward	5'-AAAGCCTTCGCTGACATGATG-3'
	Reverse	5'-ATCTCGGTGCAGTTAGTGAAGCT-3'
Calcrl (CLR)	Probe	5'-ATCGTGGTGGCTGTGTTTGCGGAG-3'
	Forward	5'-AGGCGTTTACCTGCACACACT-3'
	Reverse	CAGGAAGCAGAGGAAACCCC-3'
Nppa (ANP)	Forward	5'-TCCATCACCCTGGGCTTCT-3'
	Reverse	5'-AGGATTTGGTCCAATATGGCC-3'
Nppb (BNP)	Forward	5'-TCCAGAGCAATTCAAGATGCA-3'
	Reverse	5'-GTCTTTTCATTGCCGCTTCC-3'
Myh6 (αMHC)	Forward	5'-GCTGACAGATCGGGAGAATCAG-3'
	Reverse	5'-GCTGGCAAAGTCCTGGATGA-3'
Myh7 (βMHC)	Forward	5'-AGGGCGACCTCAACGAGAT-3'
	Reverse	5'-AGCAGACTCTGGAGGCTCTTCA-3'
Ppargc1a (PGC-1α)	Forward	5'-GGCACGCAGCCCTATTCA-3'
	Reverse	5'-CGACACGGAGAGTTAAAGGAAGA-3'
Ppargc1b (PGC-1β)	Forward	5'-CCTCTCCAGGCAGGTTCAAC-3'
	Reverse	5'-GGCCAGAAGTTCCCTTAGGATAG-3'
Ppara (PPAR-α)	Forward	5'-GGGATTGTGCACGTGCTTAA-3'
	Reverse	5'-TTTGGGAAGAGGAAGGTGTCA-3'
Atp5b (ATP synthase)	Forward	5'-AGGCTATCTATGTGCCTGCTGAT-3'
	Reverse	5'-GCATCCAAATGGGCAAAGG-3'
Bax	Forward	5'-AGACACCTGAGCTGACCTTGGA-3'
	Reverse	5'-GAGACACTCGCTCAGCTTCTTG-3'
Bcl2	Forward	5'-TGTGAGGACCCAATCTGGAAA-3'
	Reverse	5'-TTGCAATGAATCGGGAGTTG-3'

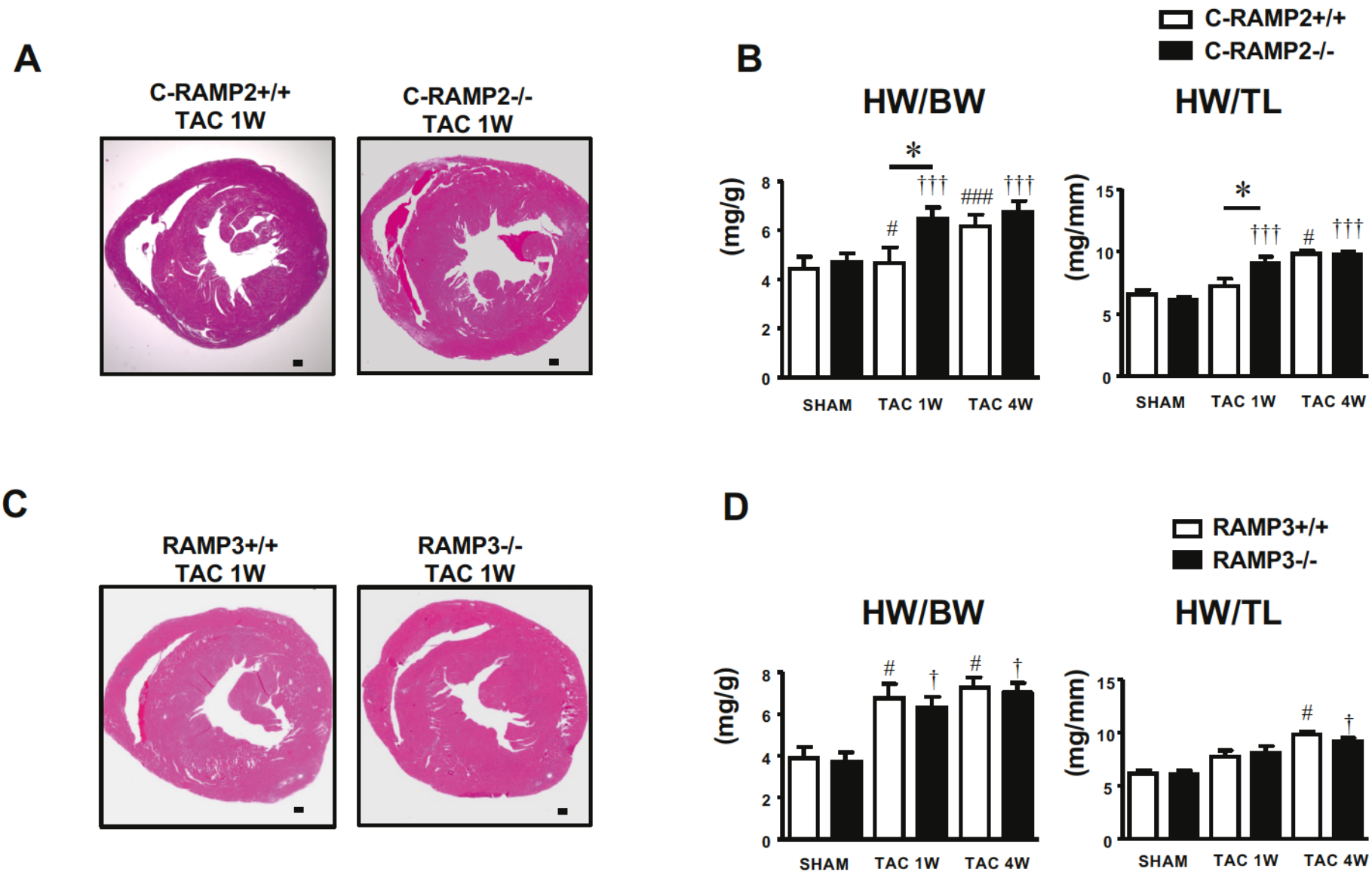

Figure 1

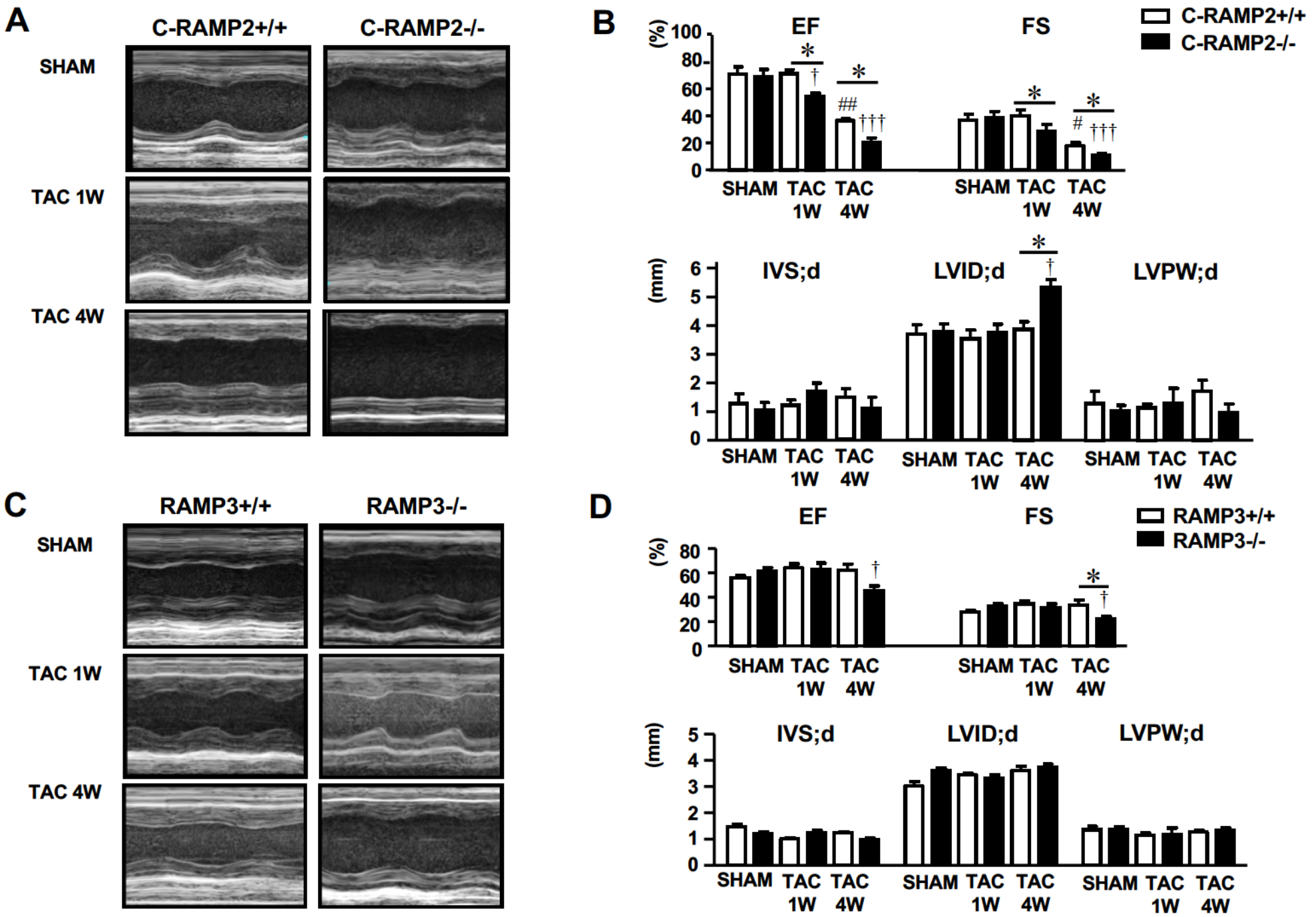

Figure 2

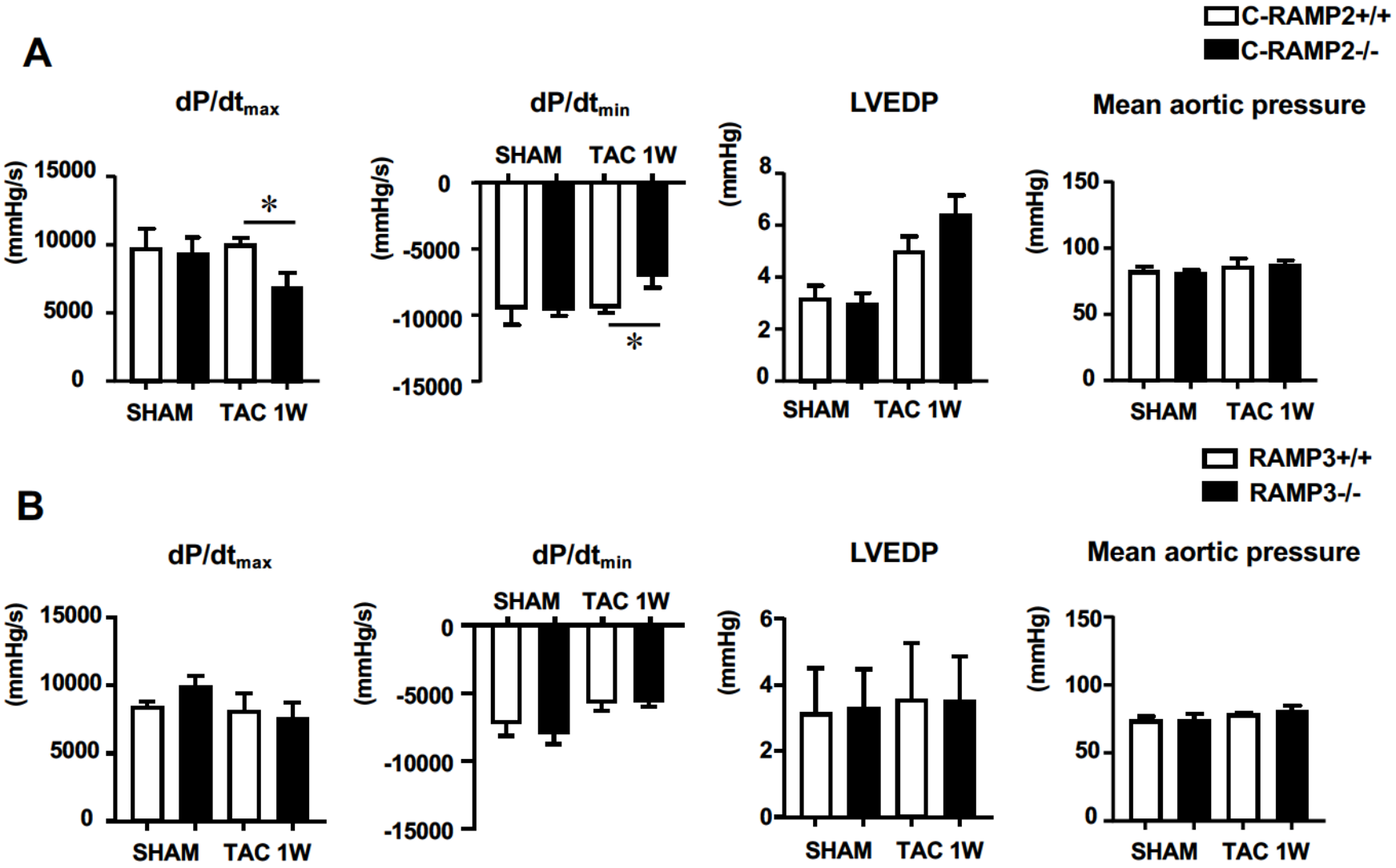

Figure 3

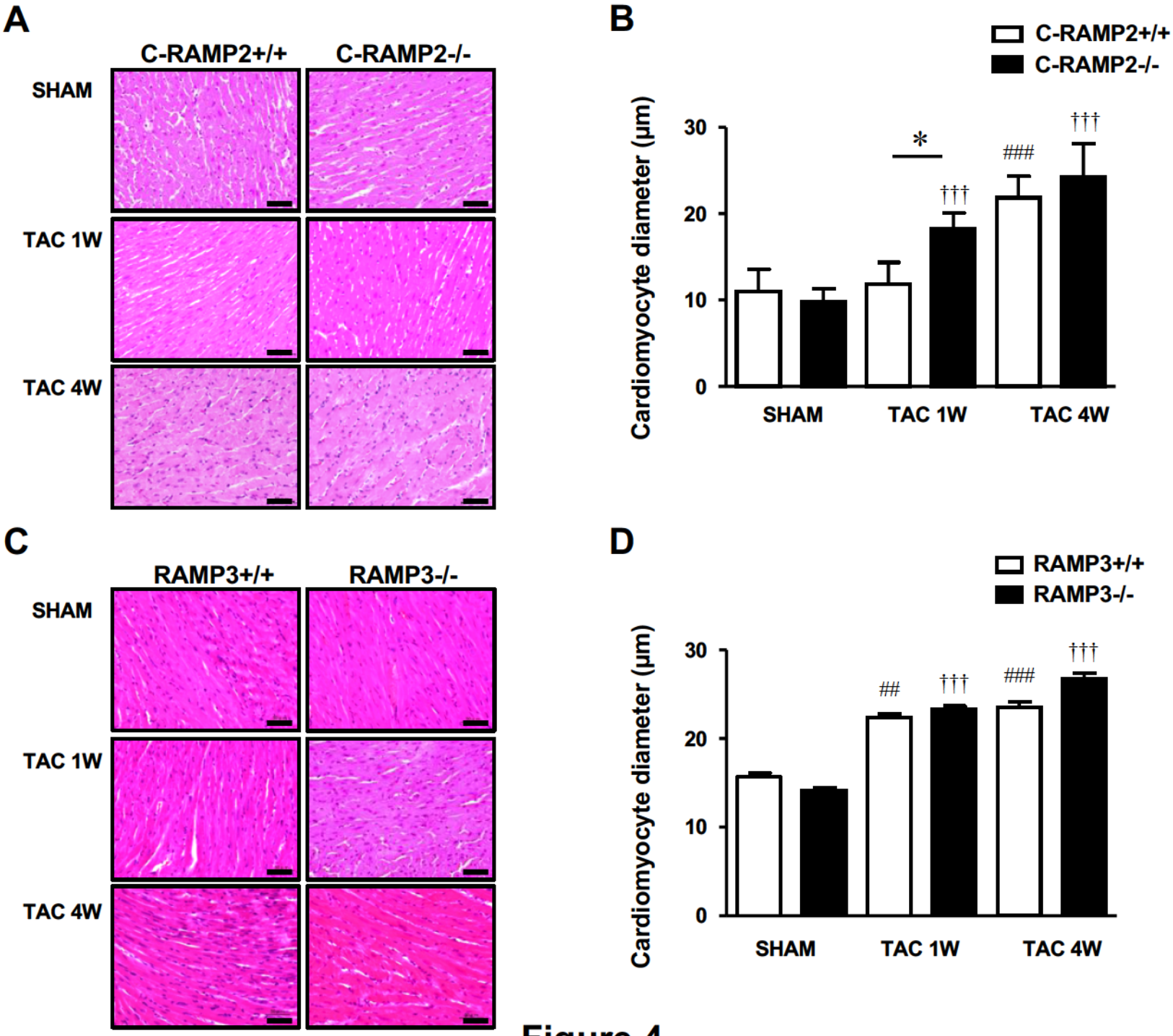

Figure 4

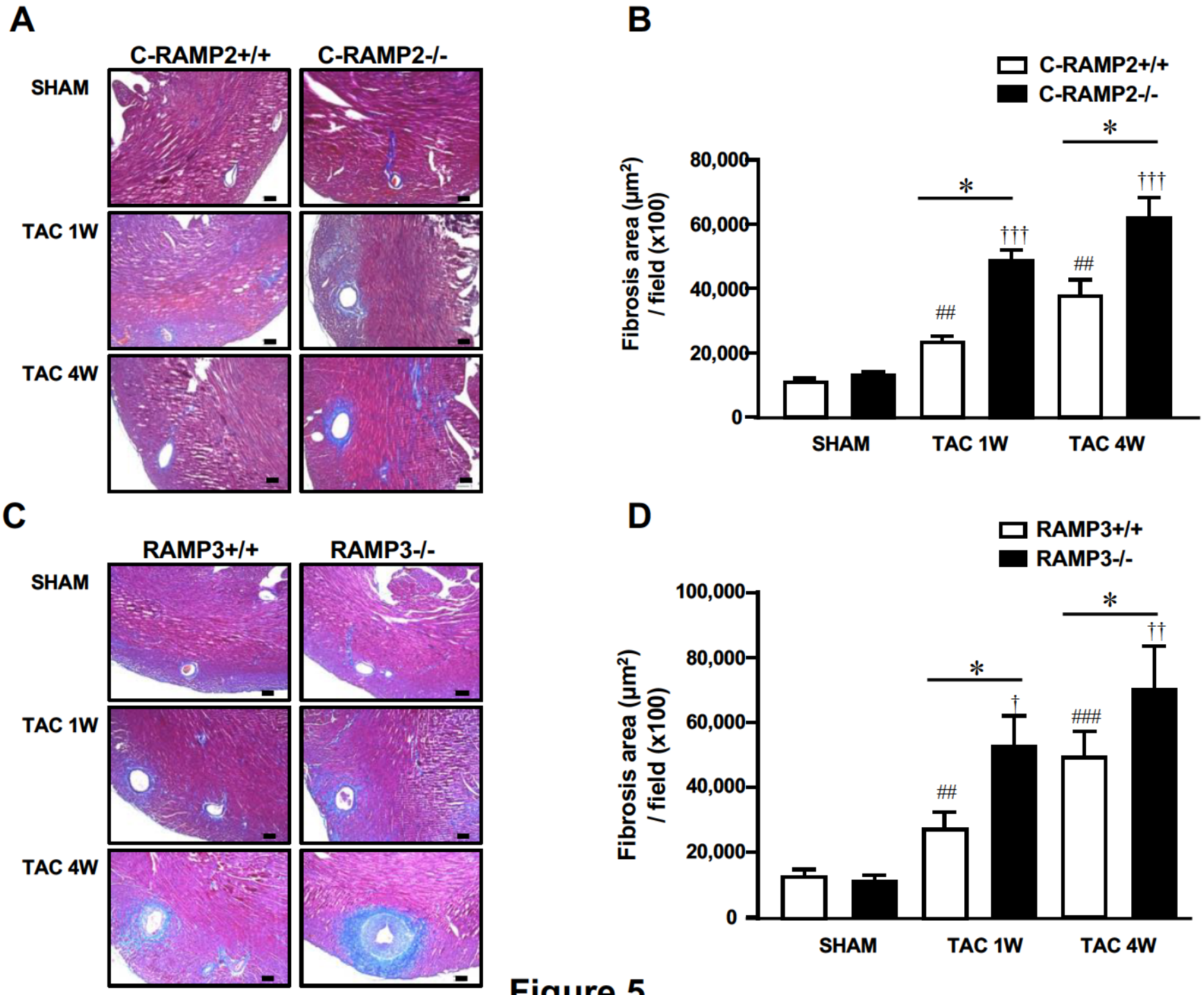

Figure 5

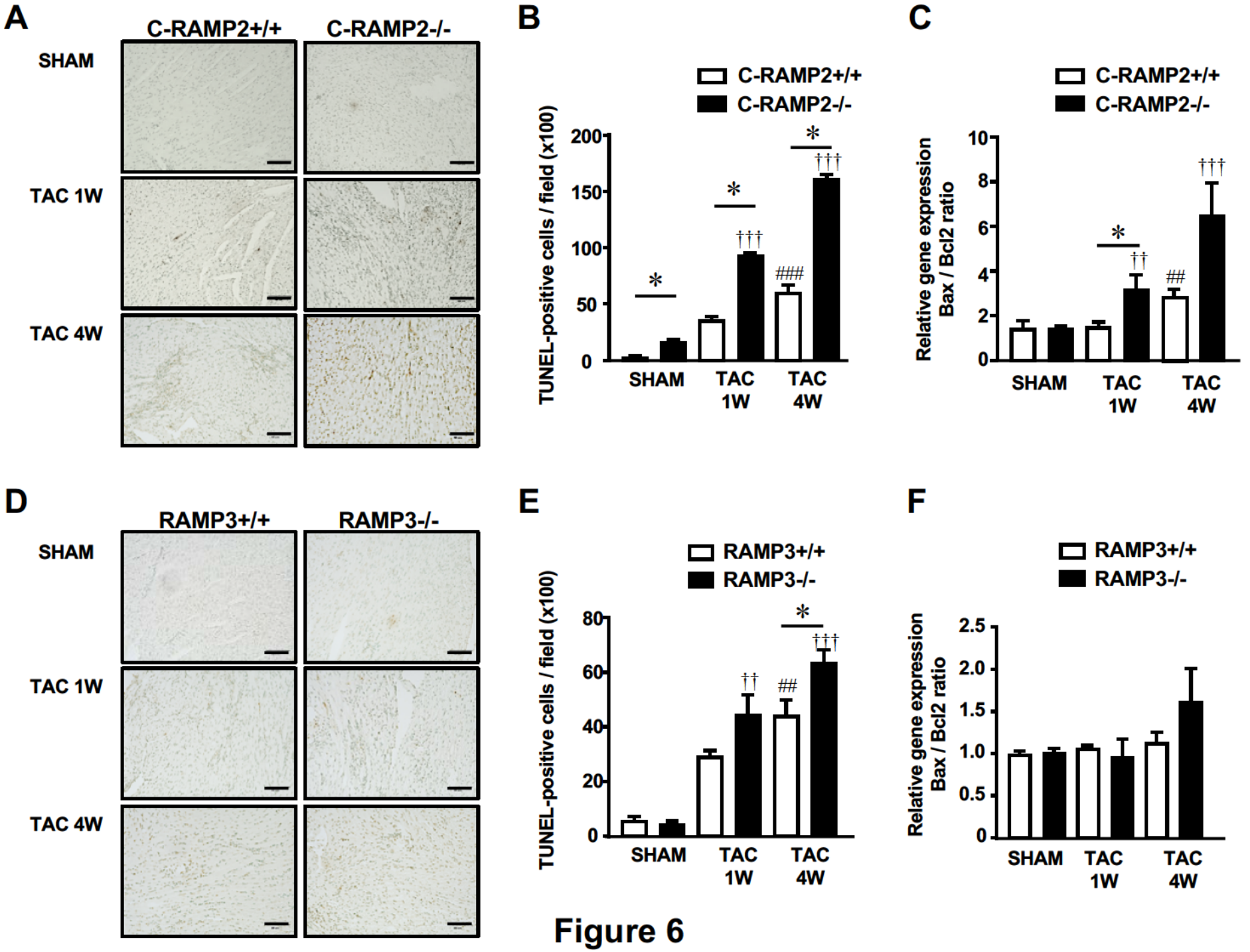

Figure 6

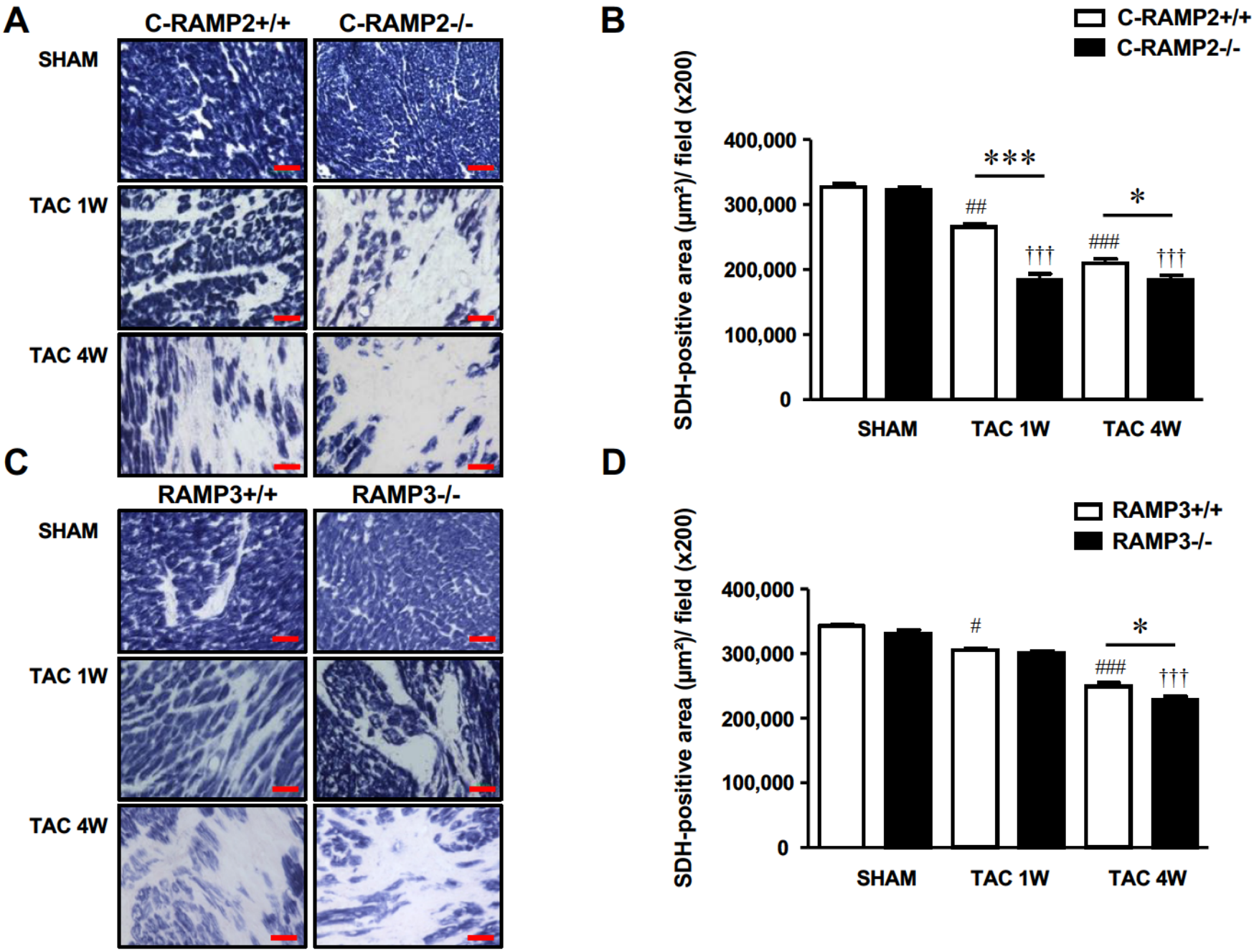

Figure 7

Figure 8

Click here to access/download;Figure;Figures 8.pdf

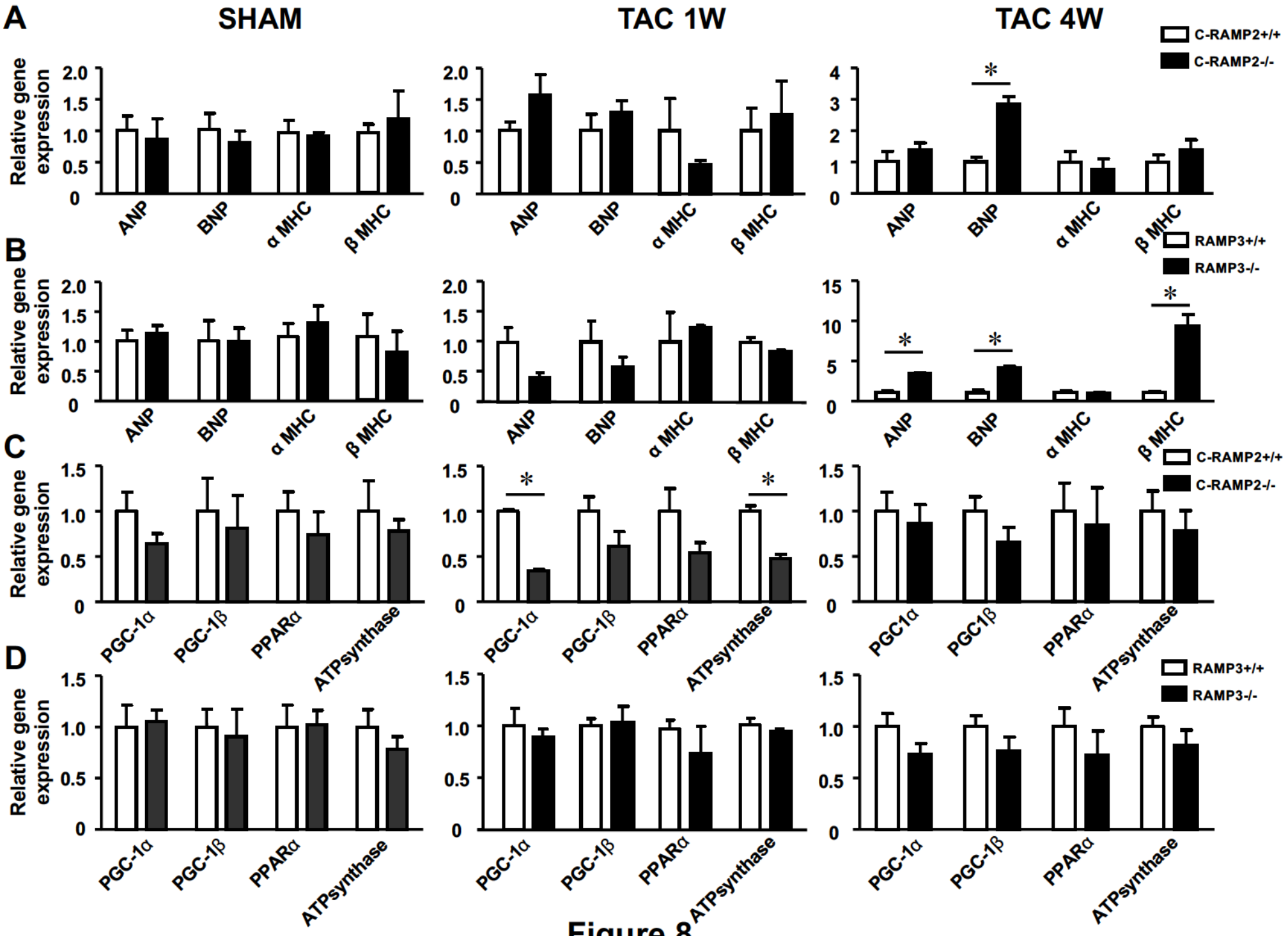

Figure 8

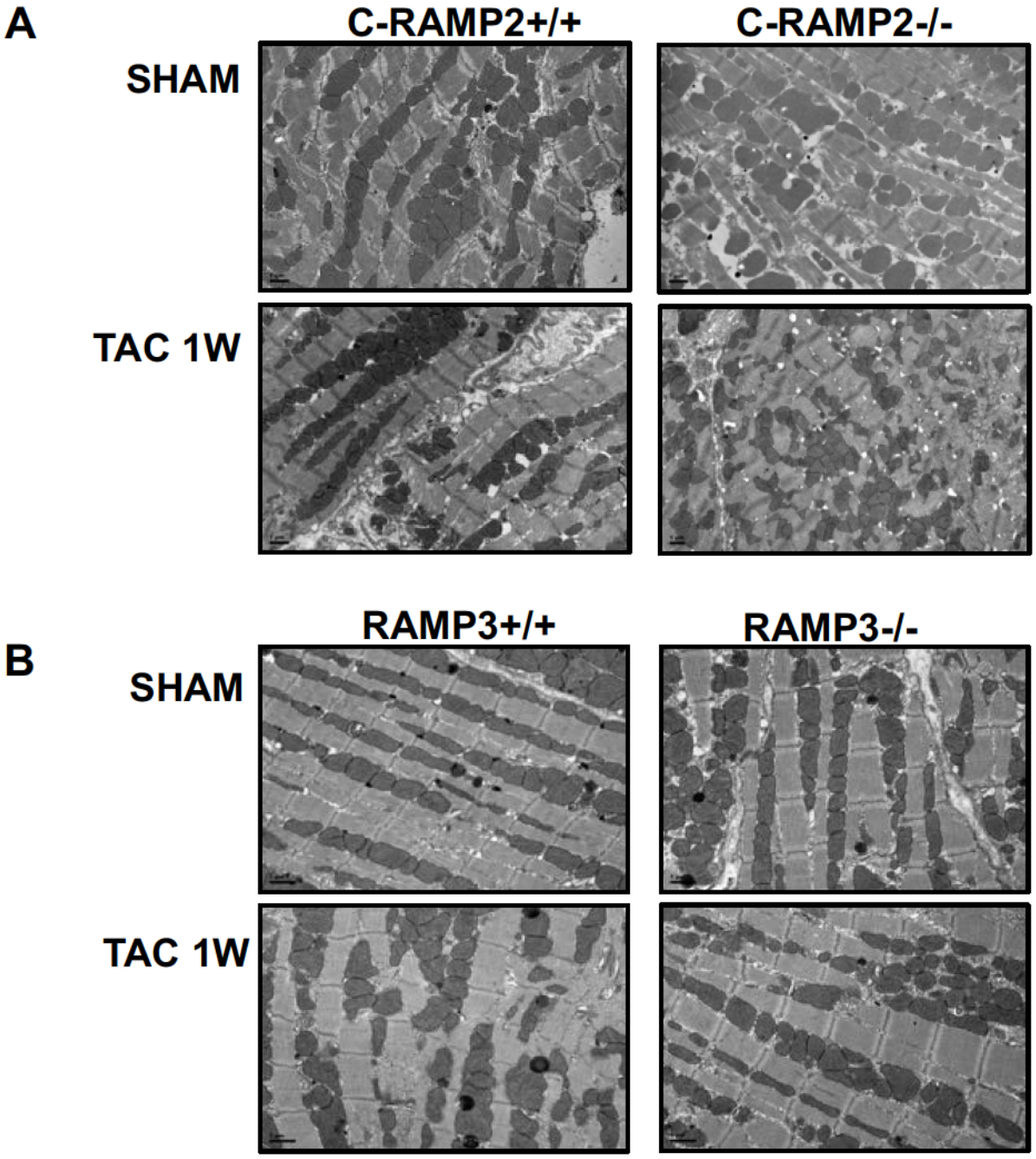

Figure 9

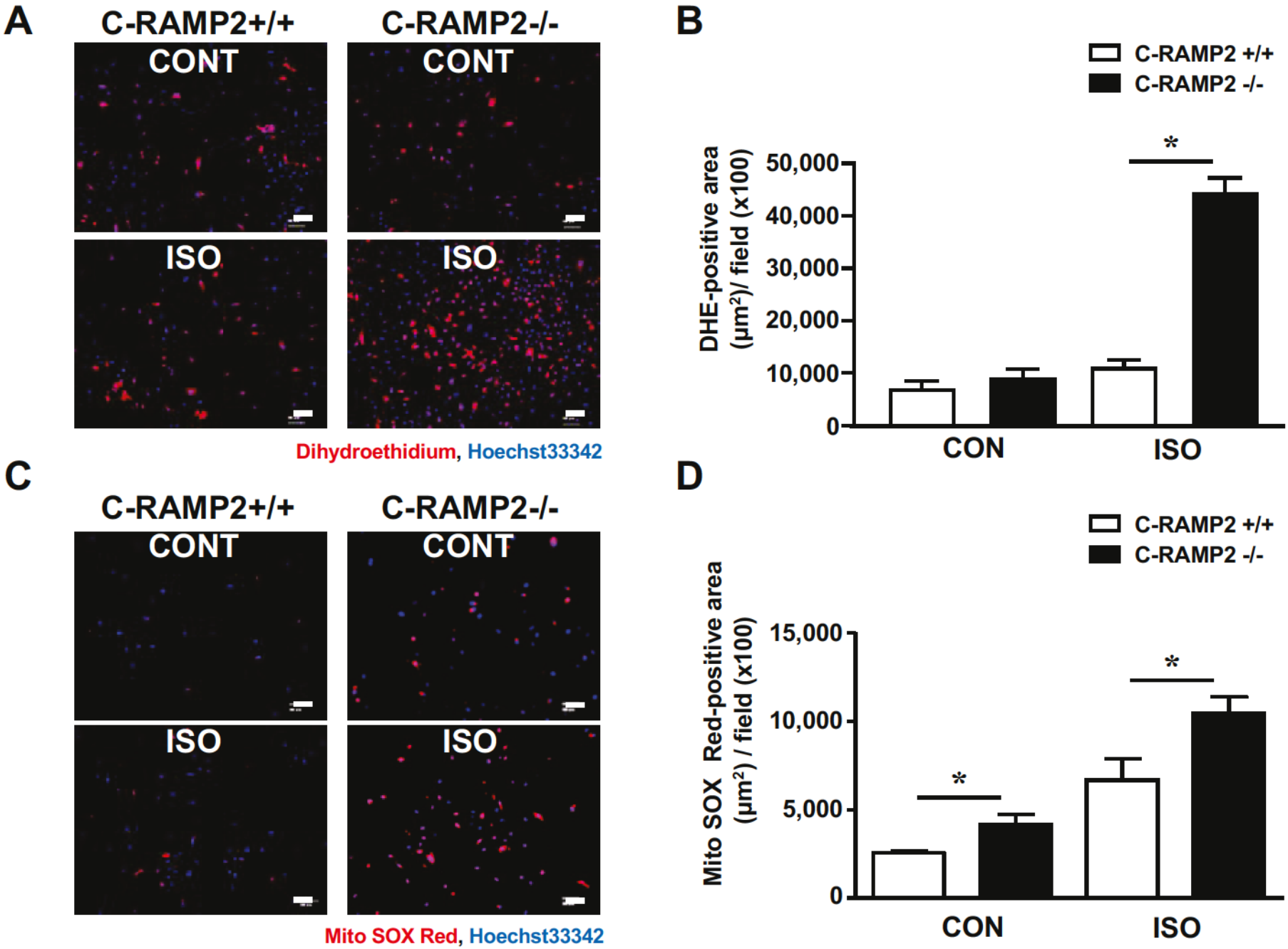

Figure 10

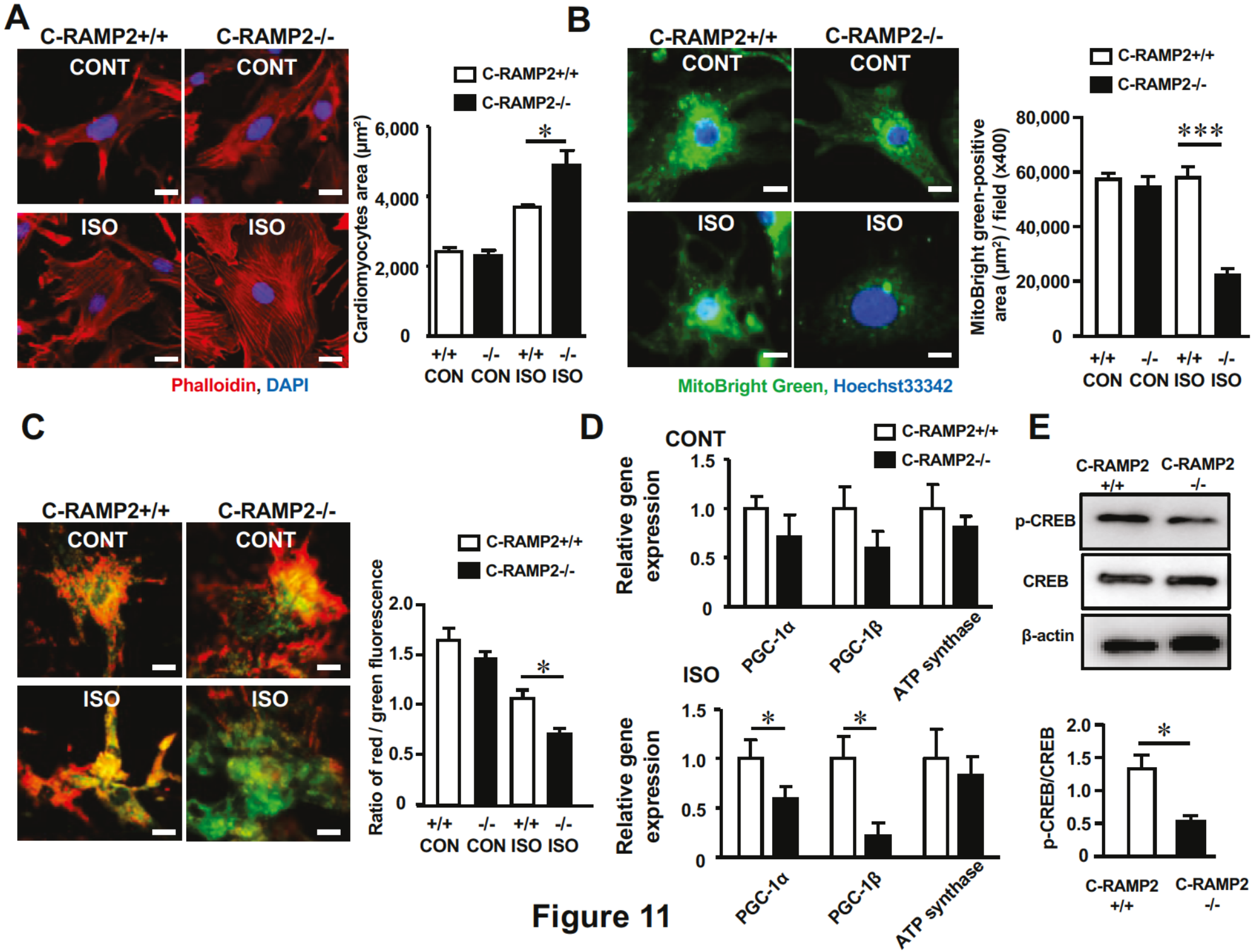

Figure 11

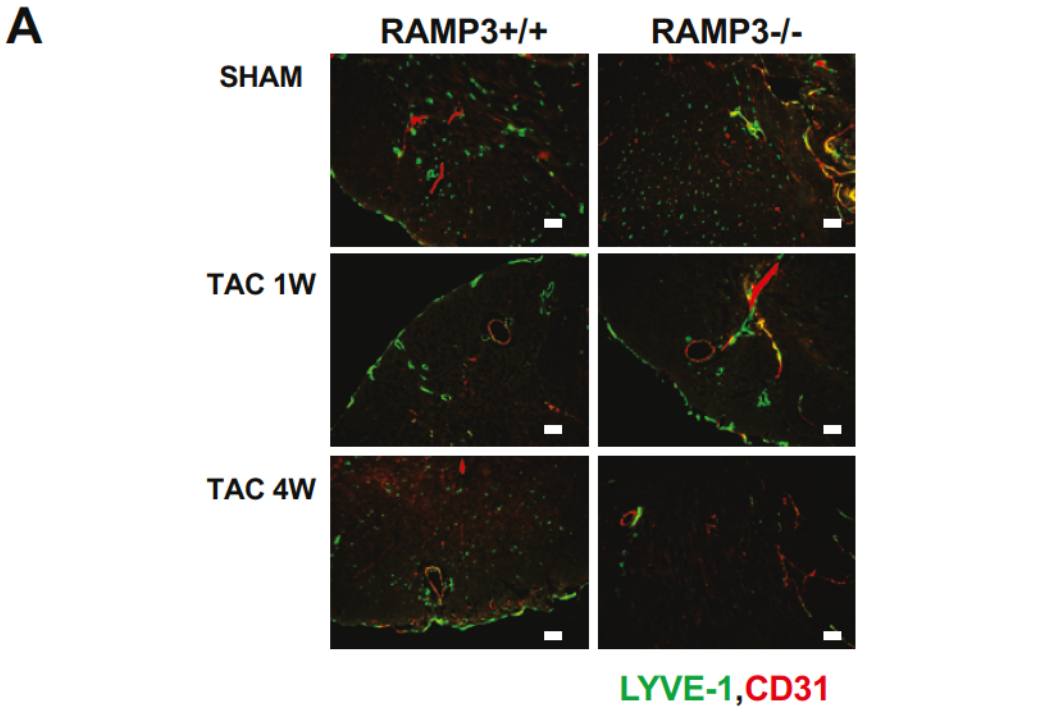

Figure 12

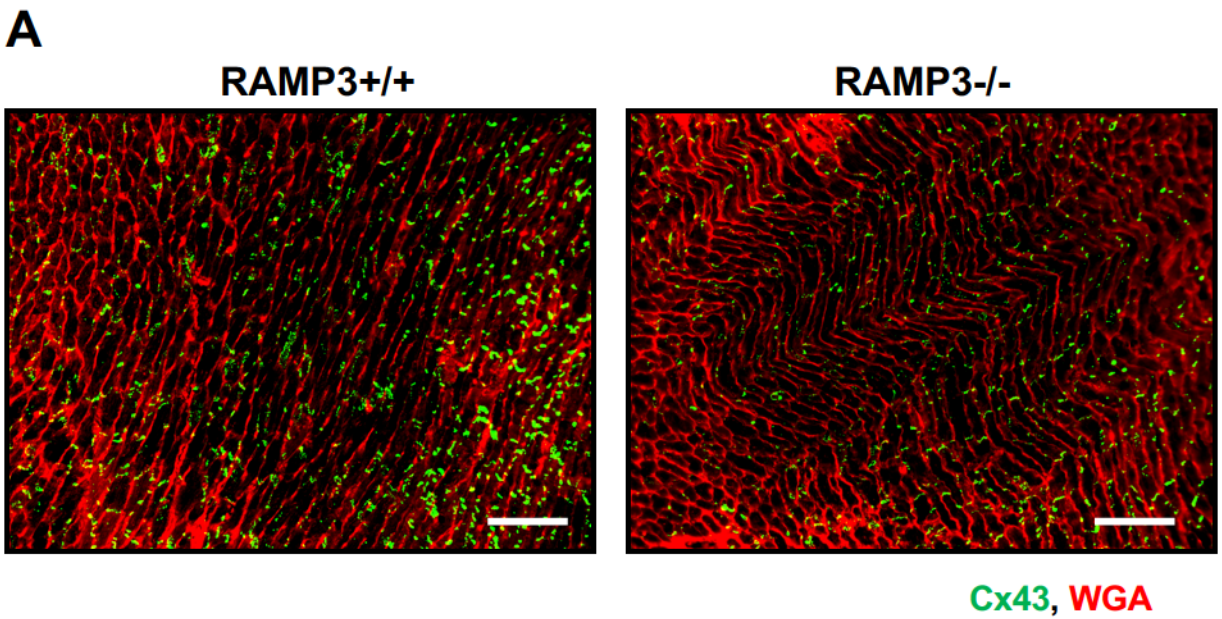

Figure 13

Figure 14

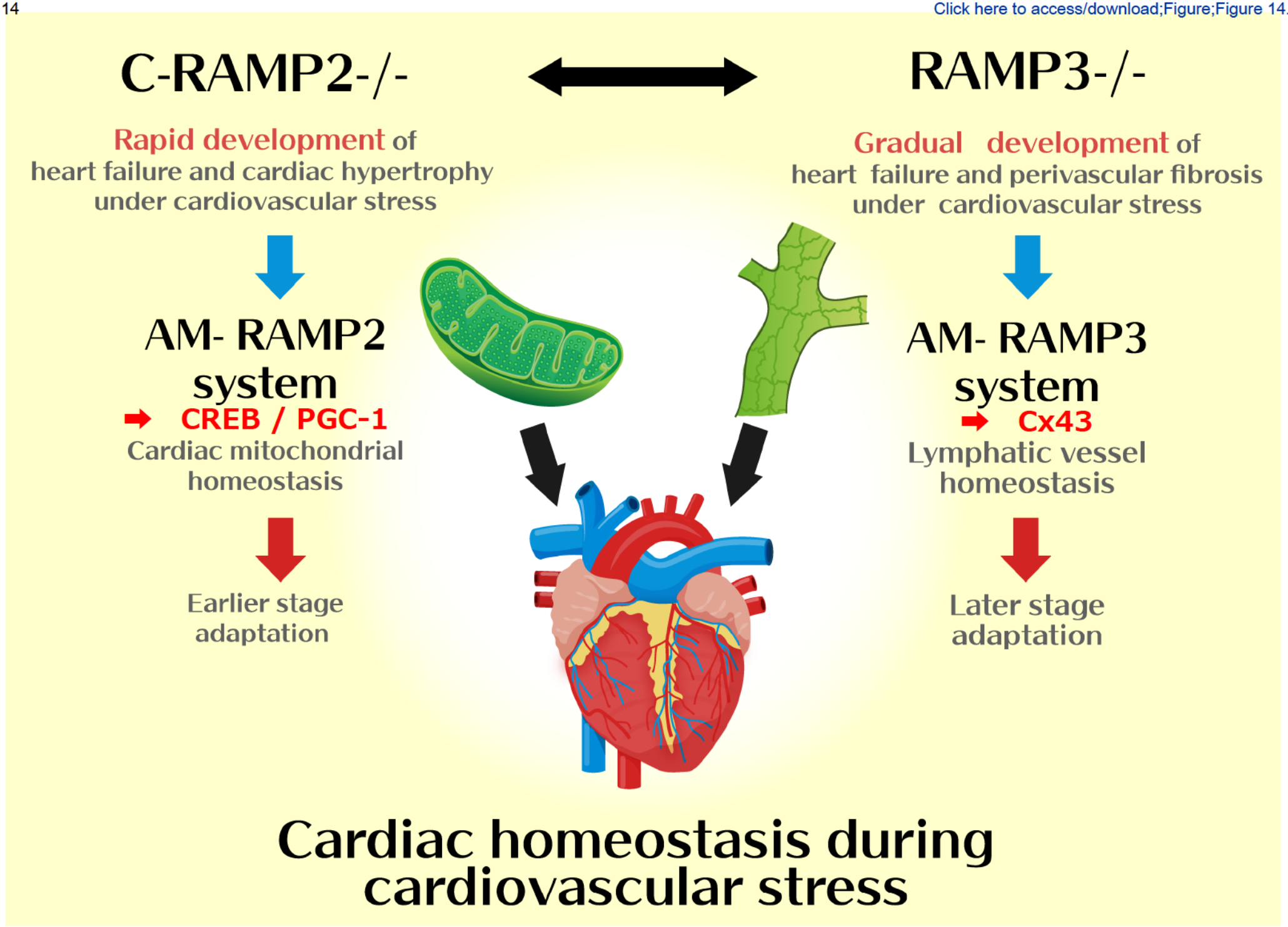

Figure 14

Supplementary Figure Legends

Supplementary Figure 1

Morphology and function of the heart before and after TAC was not different between αMHC-Cre (+) / RAMP2 flox (-) and αMHC-Cre (-) / RAMP2 flox/flox

A: Hematoxylin and eosin stained transverse heart sections after 1 week of TAC. Scale bars = 200 μm. **B:** Heart weight / body weight (HW/BW) and heart weight / tibialis length (HW/TL) ratios. **C:** Results of echocardiography. **D:** Measurements of ejection fraction (EF), functional shortening (FS), diastolic interventricular septum (IVS;d), diastolic left ventricular dimension (LVID;d), and diastolic left ventricular posterior wall (LVPW;d). Data are expressed as means ± SEM. n = 10 in αMHC-Cre (-) / RAMP2 flox/flox; n = 4 in αMHC-Cre (+) / RAMP2 flox (-) SHAM, n = 5 in αMHC-Cre (+) / RAMP2 flox (-) TAC 1W, and n = 3 in αMHC-Cre (+) / RAMP2 flox (-) TAC 4W.

Supplementary Figure 2

Reduction of capillary vessel density after TAC in C-RAMP2-/- and RAMP3-/- hearts

A, C: Isolectin-stained heart sections from C-RAMP2-/- (**A**) and RAMP3-/- (**C**) mice and their wild-type littermates (SHAM, TAC 1W, TAC 4W). Scale bars = 100 μm. **B, D:** Numbers of isolectin-positive capillary vessels / field (x100) in heart sections from C-RAMP2-/- (**B**) and RAMP3-/- (**D**) mice and their wild-type littermates. Data are expressed as means ± SEM. n = 4 in each group. "*" represents compared between the

groups, "#" represents compared with wild-type mice SHAM, "†" represents compared with knockout mice SHAM (Two-way ANOVA with Tukey's test).

Supplementary Figure 3

Cardiac expression of AM and its receptor components

Real-time PCR analysis of AM, CLR, RAMP2 and RAMP3 expression in P0 neonatal cardiomyocytes isolated from C-RAMP2-/- mice and their wild-type littermates (C-RAMP2+/+). Data are expressed as means ± SEM. n = 5 in each group. "*" represents compared between the groups (Student's t-test).

Supplementary Figure 4

TAC-induced changes in twitch Ca^{2+} transients in isolated cardiomyocytes from C-RAMP2-/-

A: Representative recordings of cytosolic Ca^{2+} transients evoked by electric pacing of single cardiomyocytes. **B:** The peak Ca^{2+} response (△F/F0); i.e., the ratio of cytosolic Ca^{2+} fluorescence evoked by electric pacing (△F) to the basal cytosolic Ca^{2+} fluorescence without stimulation (F0). Data are expressed as means ± SEM. n = 4 in each group. "*" represents compared between the groups, "#" represents compared with wild-type mice SHAM, "†" represents compared with knockout mice SHAM (Two-way ANOVA with Tukey's test).

Supplementary Figure 5

Oxidative stress was unchanged in primary cultured neonatal cardiomyocytes from RAMP3-/- mice

Cardiomyocytes were isolated from P0 RAMP3-/- or wild-type neonates, cultured for 72 h and then stimulated for 24 h with 10 μM ISO or control medium (CONT). **A, C:** Dihydroethidium (cytosolic superoxide indicator) (**A**) and MitoSOX™ Red (mitochondrial superoxide indicator) (**C**) staining in primary cultured cardiomyocytes. Scale bars = 100 μm. **B, D:** Dihydroethidium-positive (**B**) and MitoSOX™ Red-positive (**D**) areas (μm^2) / field (x100) in primary cultured cardiomyocytes. Data are expressed as means ± SEM. n = 4 in each group.

Supplementary Figure 6

Mitochondrial function was unchanged in primary cultured neonatal cardiomyocytes from RAMP3-/- mice

Cardiomyocytes were isolated from P0 RAMP3-/- or wild-type neonates, cultured for 72 h and then stimulated for 24 h with 10 μM ISO or control medium (CONT). **A:** Phalloidin-stained cardiomyocytes showing actin filaments **(left)**. Cardiomyocyte sizes were compared between RAMP3-/- and wild-type cells (**right**). **B:** MitoBright Green-stained cardiomyocytes showing viable mitochondria **(left)**. MitoBright Green-positive areas/field (x400) were compared between RAMP3-/- and wild-type cells (**right**). **C**: JC-1-stained (mitochondrial membrane potential indicator) cardiomyocytes **(left)**. Red/green fluorescence ratios were compared between RAMP3-/- and wild-type cells (**right**). Mitochondrial depolarization is indicated by a decrease in the red/green fluorescence intensity ratio. Scale bars in **A-C** are 10 μm. Data are expressed as means ± SEM in **A-C.** n = 4. **D**: Real-time PCR analysis of the expression of mitochondria-related genes in control (CONT) and ISO-treated neonatal cardiomyocytes. The mean in wild-type cardiomyocytes was assigned a value of 1. Data

are expressed as means ± SEM. n = 5 in each group. **E,** Western blot analysis of CREB and phosphorylated (activated) CREB (p-CREB) in primary cultured cardiomyocytes. The CREB activation level is indicated by the p-CREB/CREB band intensity ratio. Data are expressed as means ± SEM. n = 3 in each group.

Supplementary Figure 7

Analysis of mitochondrial respiration (Mito stress test) in cultured neonatal cardiomyocytes from C-RAMP2-/-

The graphs show the oxygen consumption rate (OCR) during the indicated treatments. Cardiomyocytes were isolated from P0 C-RAMP2-/- or wild-type neonates and stimulated for 24 h with 10 μM ISO or control medium (CONT). Mitochondrial respiration was measured through chronological injections of oligomycin, FCCP, antimycin A and rotenone to assess basal respiration, maximal respiration, spare respiratory capacity and ATP production. **A, B:** Time course (**A**) and quantitative statistical analysis (**B**) of OCR in control medium. **C, D:** Time course (**C**) and quantitative statistical analysis (**D**) of OCR in the presence of ISO. Data are expressed as means ± SEM. n = 3 in each group. "*" represents compared between the groups (Student's t-test).

Supplementary Figure 8

Lymphatic vessel density was unchanged in C-RAMP2-/- hearts

A: LYVE-1- and CD31-immunostained heart sections from C-RAMP2-/- mice and their wild-type littermates (SHAM, TAC 1W, TAC 4W). (green = LYVE-1, red = CD31). Scale bars = 100 μm. **B:** Comparison of the numbers of lymphatic vessels/field (x100)

in heart sections from C-RAMP2-/- mice and their wild-type littermates. Data are expressed as means ± SEM. n = 4 in each group.

Supplementary Figure 9

Cx43 localization was unchanged in C-RAMP2-/- hearts

A: Cx43-immunostained heart sections from C-RAMP2-/- mice and their wild-type littermates (TAC 4W). (green = Cx43, red = WGA). Scale bars = 100 μm. **B:** Comparison of the Cx43-positve area (μm^2)/field (x 200) in heart sections from C-RAMP2-/- mice and their wild-type littermates. Data are expressed as means ± SEM. n = 4 in each group.

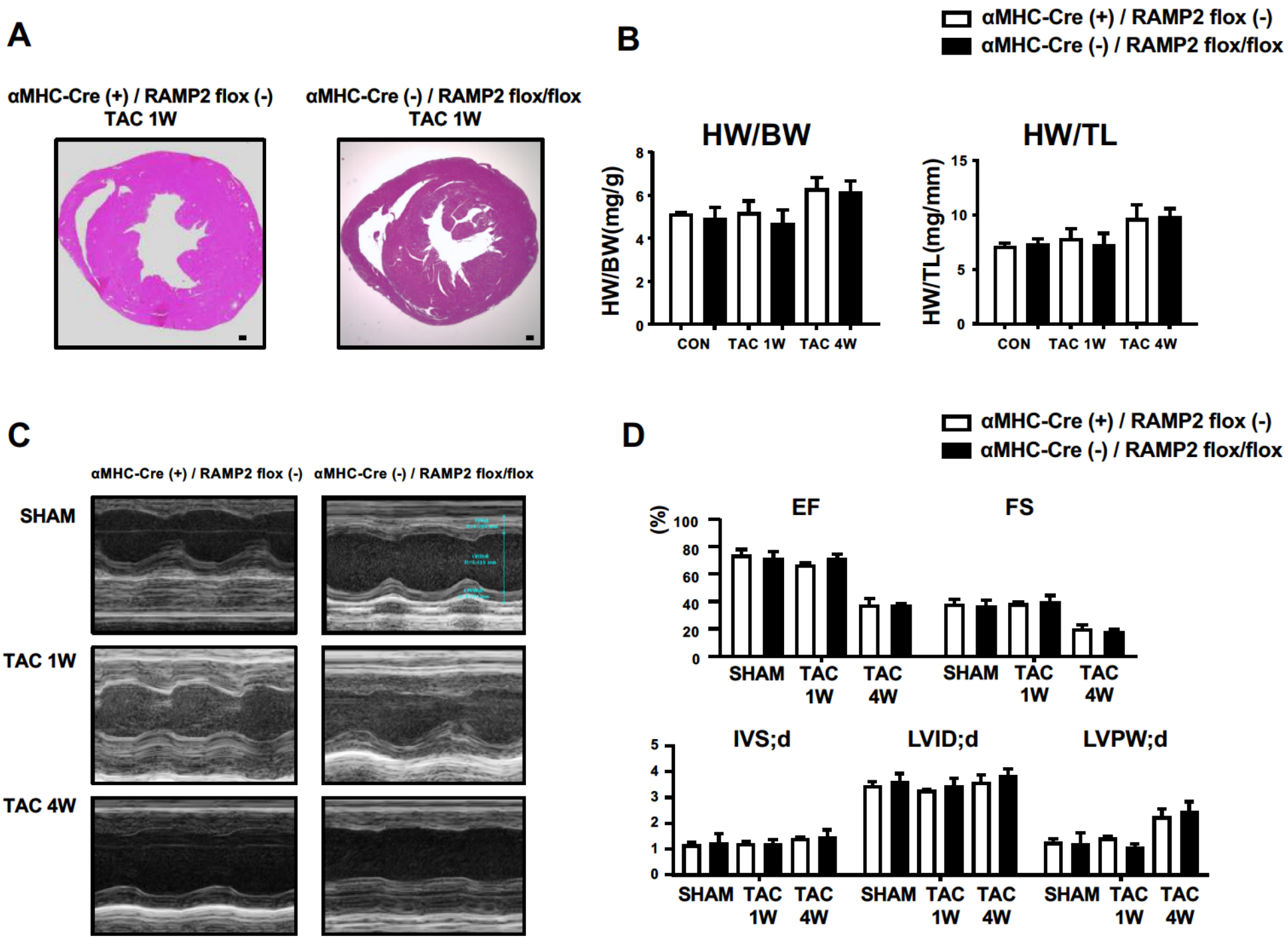

Supplementary Figure 1

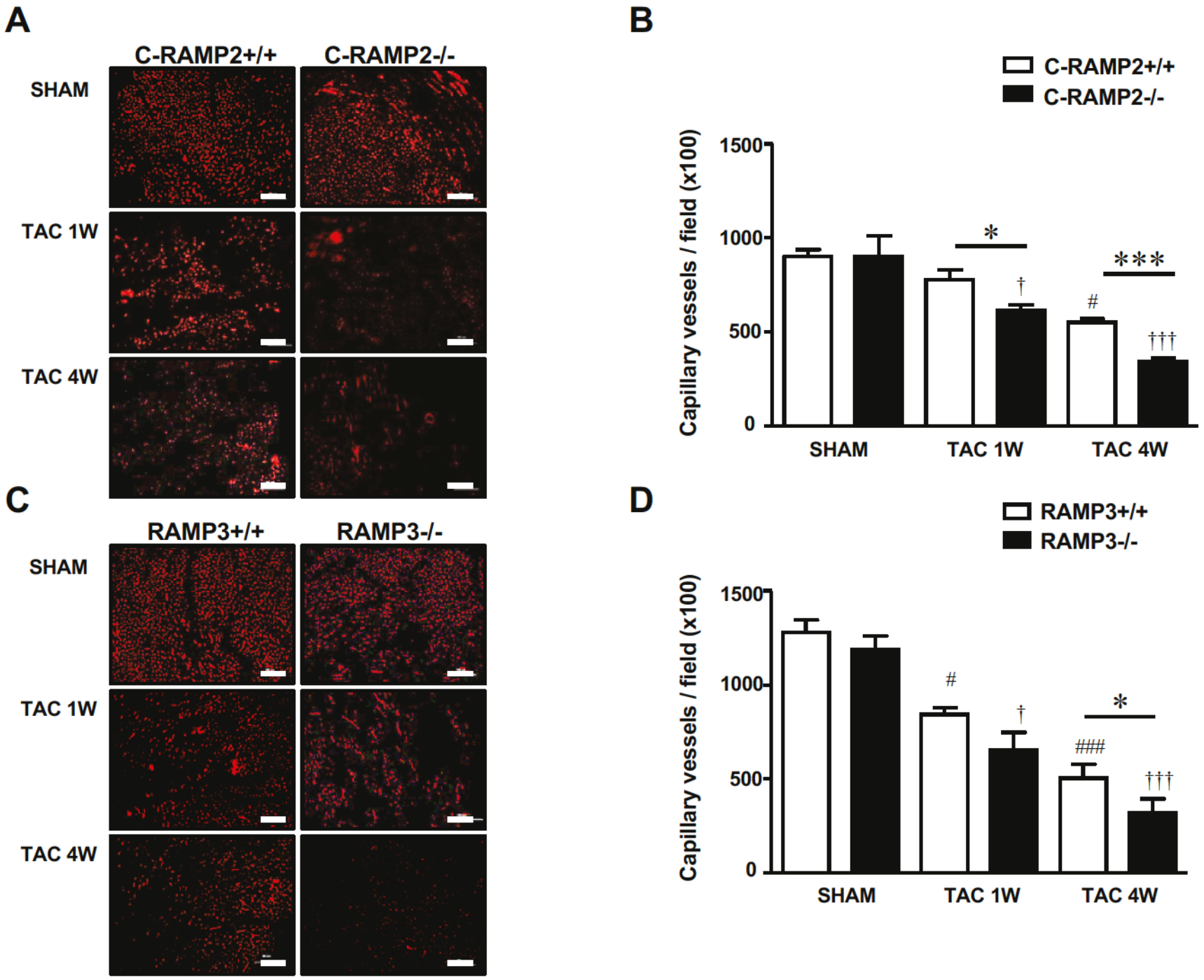

Supplementary Figure 2

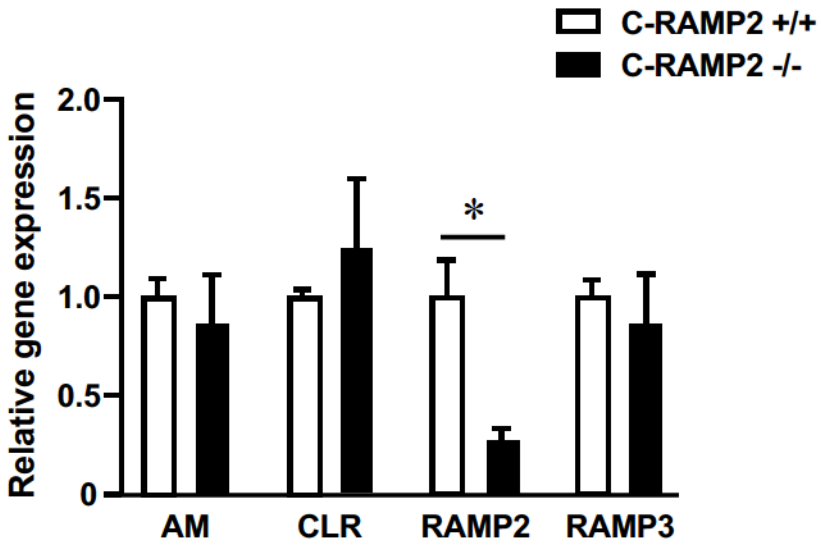

Supplementary Figure 3

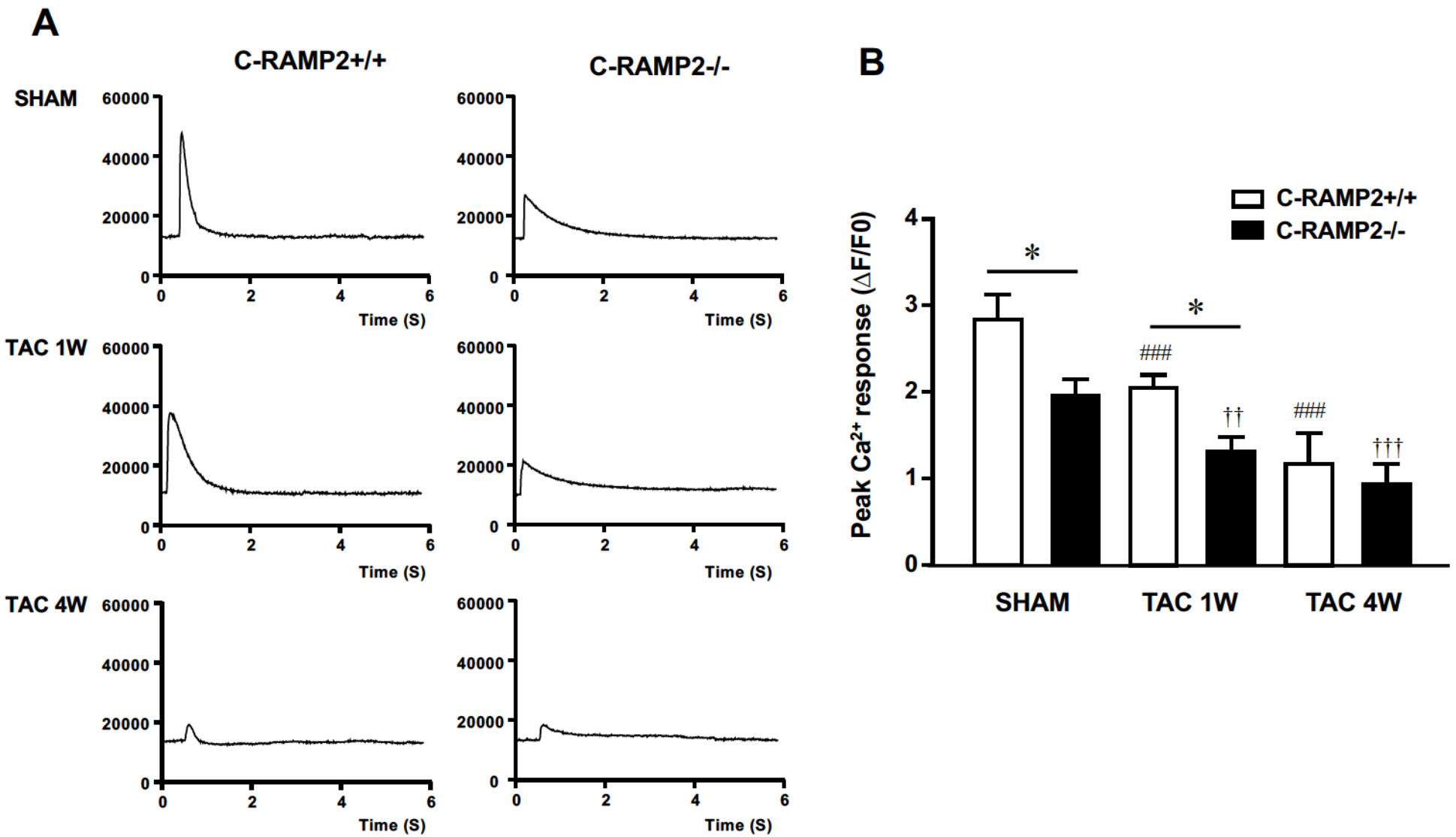

Supplementary Figure 4

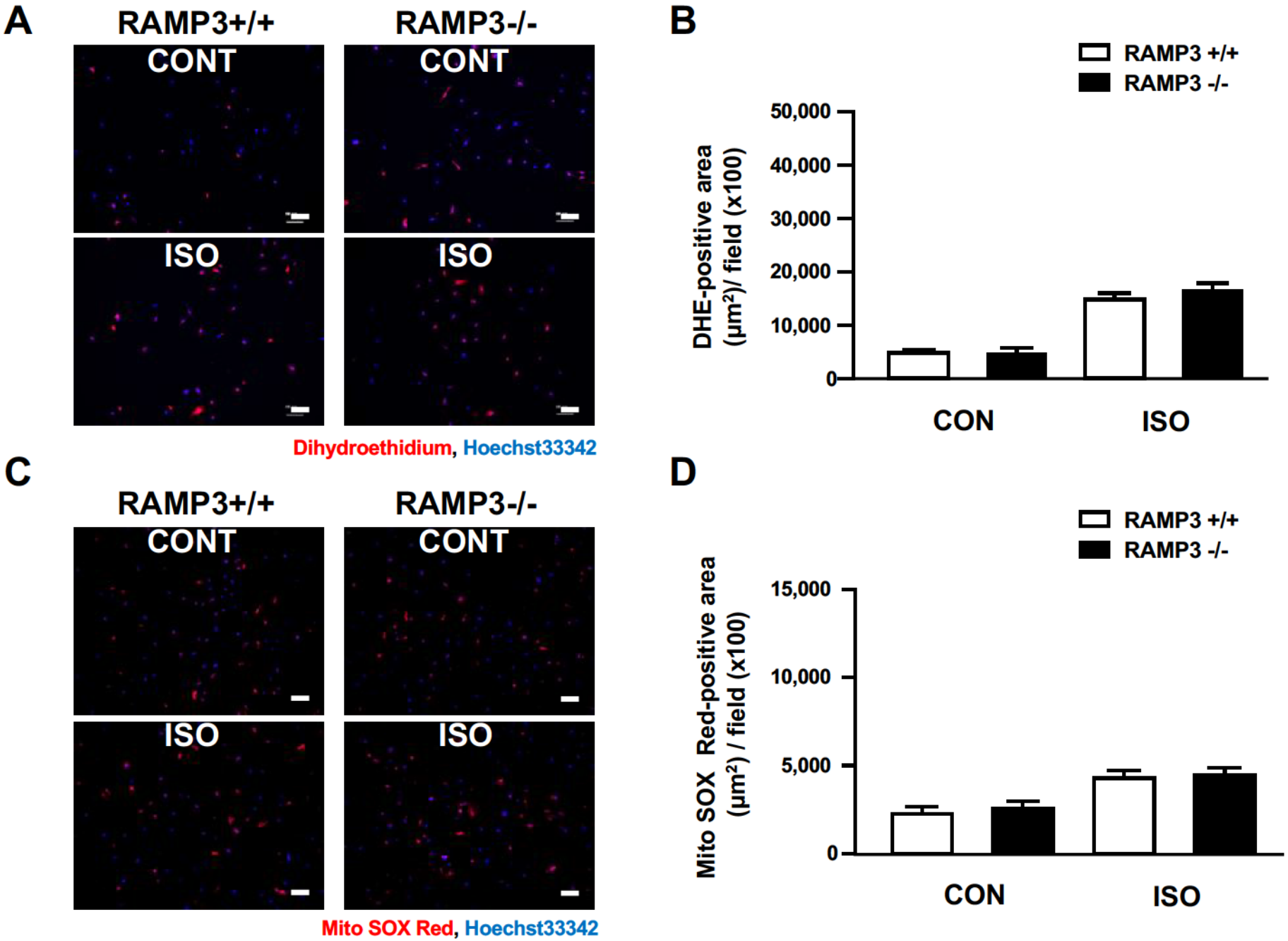

Supplementary Figure 5

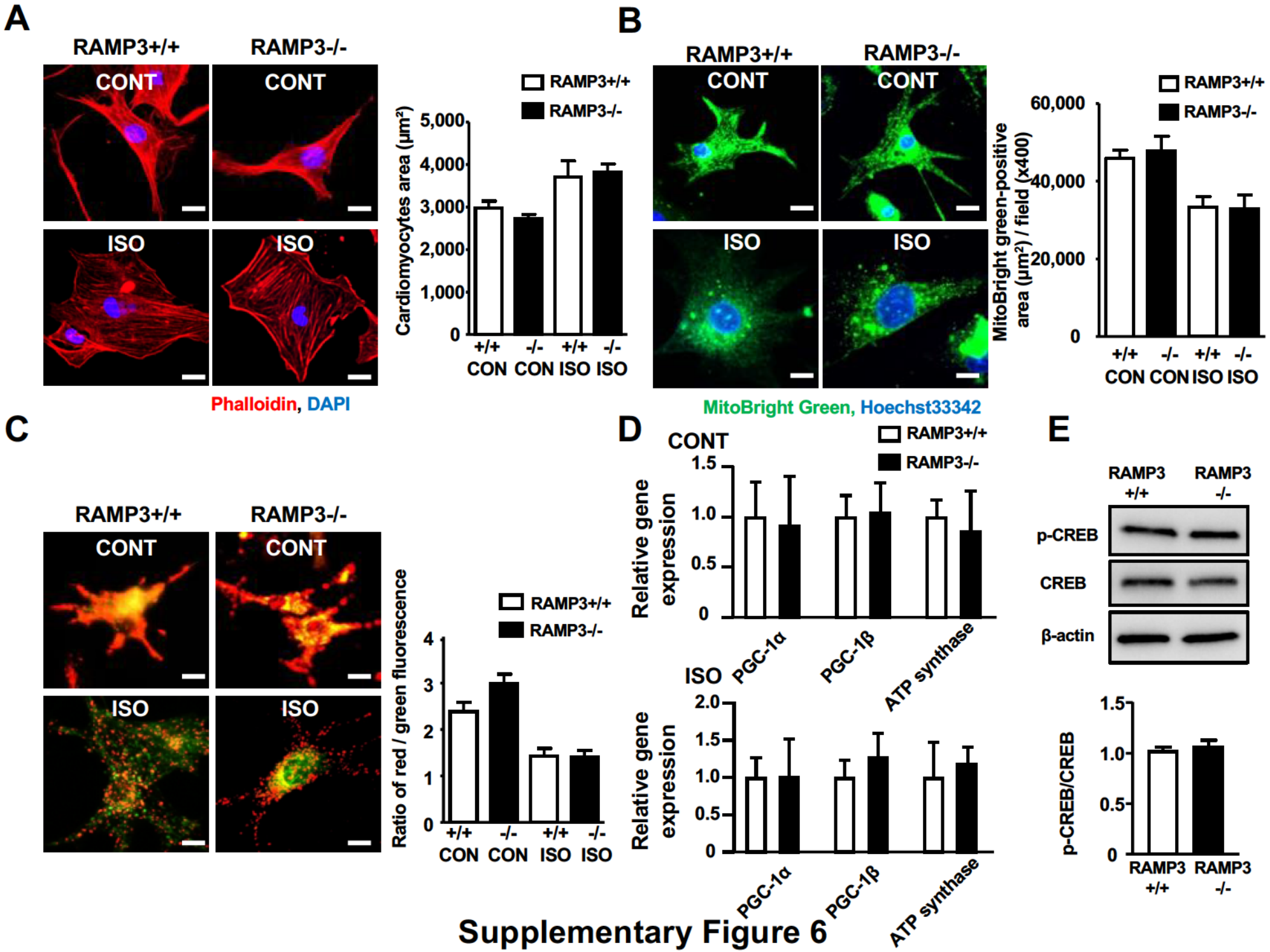

Supplementary Figure 6

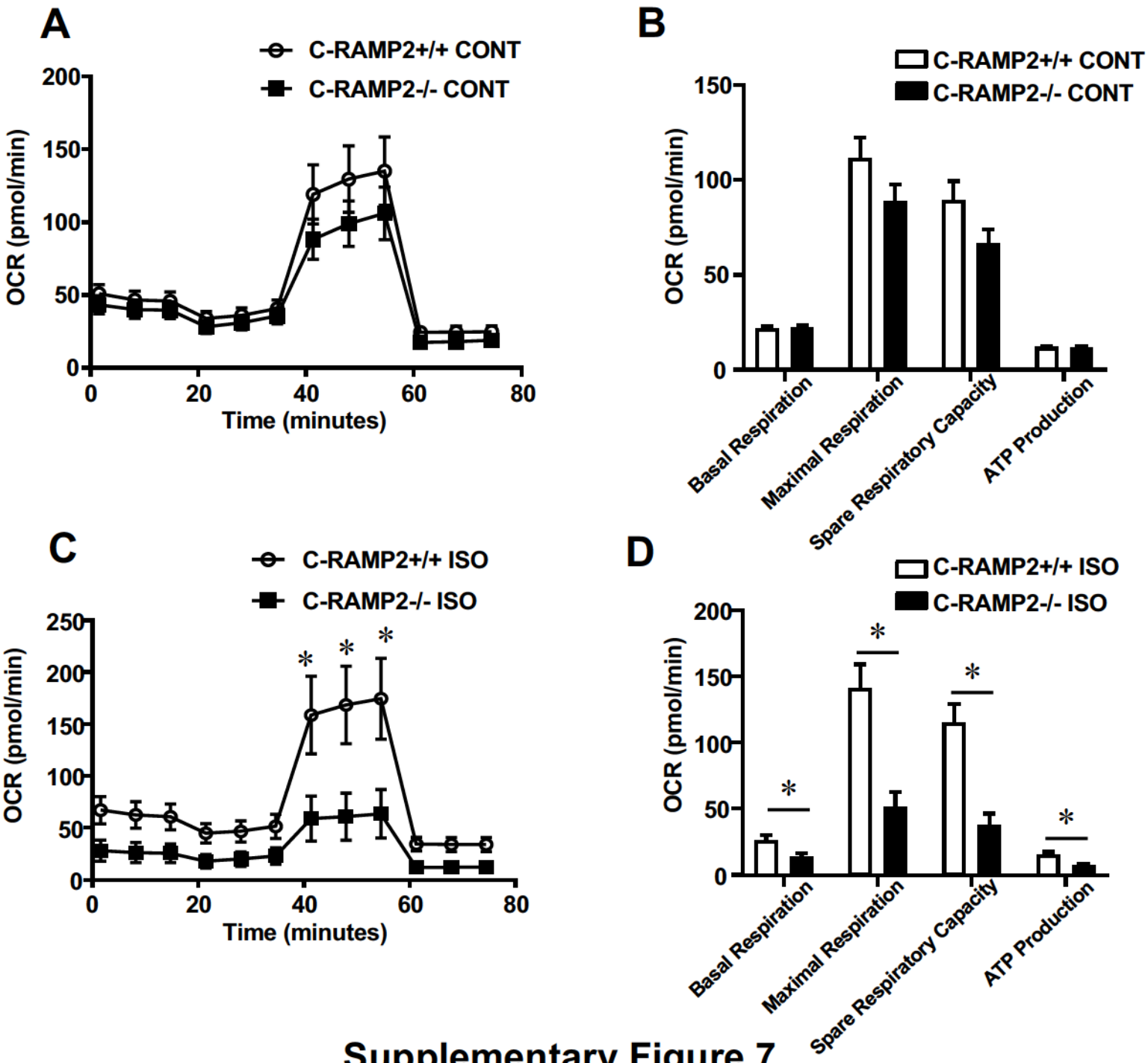

Supplementary Figure 7

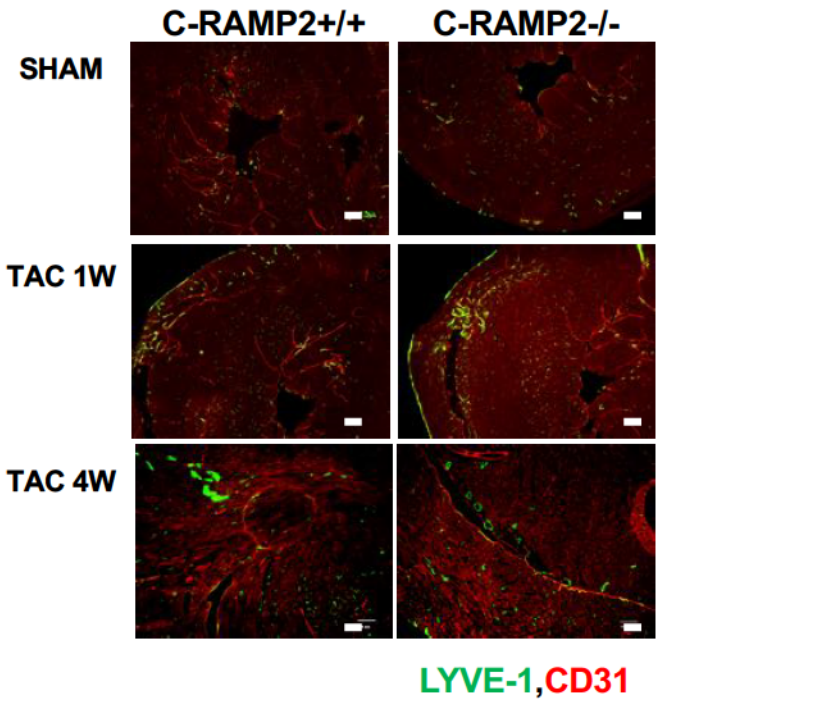

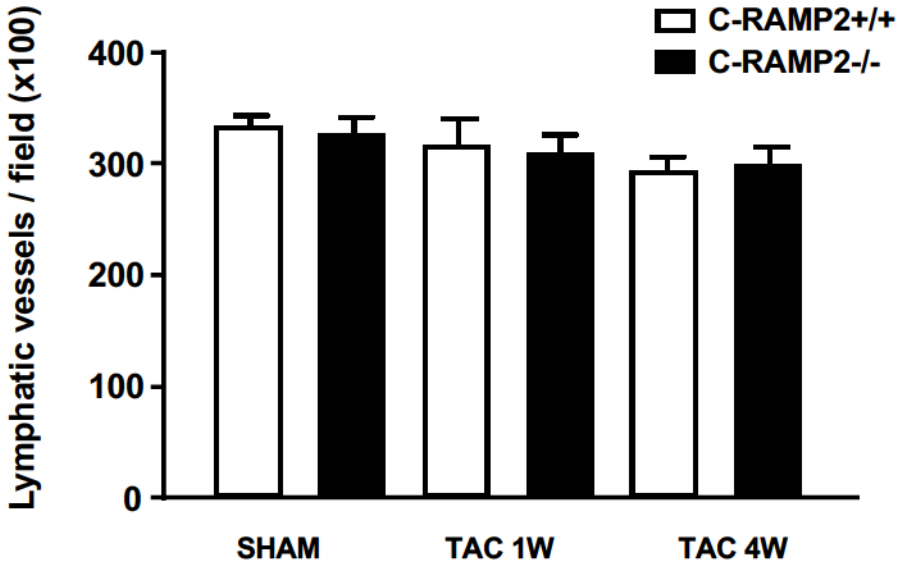

Supplementary Figure 8

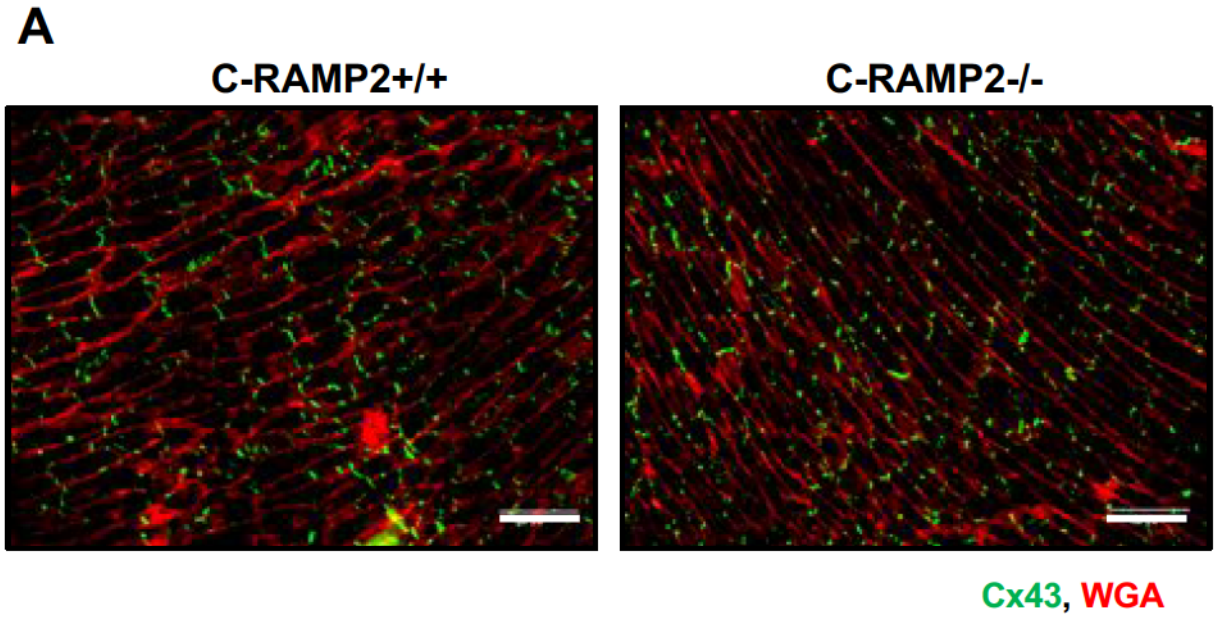

Supplementary Figure 9